Aalto University
School of Electrical Engineering

Hannes Hyvönen

Thermomechanical and Mechanical Characterization of a 3-Axial MEMS Gyroscope

Master's Thesis
Espoo, August 9, 2011

Supervisor: Prof. Mervi Paulasto-Kröckel D.Sc. (Tech.)
Instructor: Docent Toni Mattila D.Sc. (Tech.)

Aalto University
School of Electrical
Engineering

Aalto University
School of Electrical Engineering

ABSTRACT OF THE MASTER'S THESIS

Author: Hannes Hyvönen

Title of thesis: Thermomechanical and Mechanical Characterization of a 3-Axial MEMS Gyroscope

Date: August 9, 2011 **Language:** English **Pages:** 7 + 77

Department of Electronics
Professorship: Electronics integration and reliability **Code:** S-113
Supervisor: Prof. Mervi Paulasto-Kröckel D.Sc. (Tech.)
Instructor: Docent Toni Mattila D.Sc. (Tech.)

The purpose of this thesis was to develop automated, efficient and economical methods for the mechanical and thermomechanical characterization of a digital 3-axial microelectromechanical systems (MEMS) gyroscope. The development of the test equipment and methods was the emphasis of this thesis, but the failure analyses of MEMS gyroscopes are beyond the scope of this work. A gyroscope is a device for measuring angular velocity and sensing change in orientation around its X, Y and Z-axis. The experimental part is divided into two sections, of which the first one is focused on high-G shock impact and vibration loading and the second on thermomechanical characterization.

A rotation device was developed for the characterization of the MEMS gyroscopes in a temperature and humidity chamber. The rotation device consists of a one-axial servo-motor, a servo-drive and a control program for the readout of angular velocity. The device is capable of simultaneously recording the angular velocities of the gyroscopes from all three axes while rotating the gyroscopes around a single axis. The device also records the temperature of the environment. The high-G shock impact equipment consists of a pneumatically assisted shock tester that relies on mechanical impact to generate the high-G shock pulse. An existing mechanical shock impact system was modified to gain higher G-values (up to 80000G) and to enable the inspection of gyroscopes in different orientations. The vibration test equipment consists of a waveform generator and a vibration shaker, for the vibration testing of gyroscopes. The waveform generator is capable of outputting different waveforms with different frequencies to the shaker that vibrates with the given output.

The functionality of the rotation device was tested with rotating one gyroscope board at room temperature. Respective averages and standard deviations of angular velocities were measured in the direction of X, Y and Z axes. The functionality of the high-G shock impact test equipment was verified with six measurements where all of the gyroscopes failed on first impact. The vibration test equipment was tested with one gyroscope board. Root mean square (RMS), peak value and total energy of acceleration were measured with an accelerometer placed on top of the vibrating gyroscope board.

Keywords: Gyroscope, MEMS, mechanical testing, environmental testing, reliability, characterization

Aalto-yliopisto | DIPLOMITYÖN TIIVISTELMÄ
Sähkötekniikan korkeakoulu

Tekijä: Hannes Hyvönen

Työn nimi: Kolmiakselisen MEMS Gyroskoopin Termomekaaninen ja Mekaaninen Karakterisointi

Päiväys: 9. elokuuta 2011 **Kieli:** englanti **Sivumäärä:** 7 + 77

Elektroniikan laitos

Professuuri: Elektroniikan integrointi ja luotettavuus **Koodi:** S-113

Työn valvoja: Prof. Mervi Paulasto-Kröckel

Työn ohjaaja: Dosentti Tkt. Toni Mattila

Työn tavoitteena oli automaattisten, tehokkaiden ja edullisten testauslaitteistojen ja -menetelmien kehittäminen kolmiakselisten mikroelektromekaanisten (MEMS) gyroskooppien mekaaniseen ja termomekaaniseen karakterisointiin. Työn painotuksena oli testausmenetelmien ja -laitteistojen kehittäminen ja gyroskooppien vaurioanalyysit jäävät tämän työn ulkopuolelle. Gyroskooppi on kulmanopeuden mittaamiseen ja asennon aistimiseen käytettävä anturi. Mekaaninen karakteristointi kattaa gyroskooppien korkean G-arvon iskumaiset kuormitukset ja tärinäkuormitukset. Lämpömekaaninen karakterisointi kattaa gyroskooppien ympäristöolojen kontrolloimista lämpö-, kosteus- tai monikaasu -kaapissa.

Tässä työssä kehitettiin menetelmä kolmiakselisten MEMS-gyroskooppien karakterisointiin lämpö- ja kosteuskaapissa. Menetelmä koostuu yksiakselisesta servomoottorista, servo-ohjaimesta ja ohjaussovelluksesta, jonka avulla voidaan samanaikaisesti mitata ja tallentaa gyroskooppien kulmanopeus kaikilta kolmelta (X, Y ja Z) akselilta sekä mitata ympäristön lämpötilaa. Korkean G-arvon iskumaisiin kuormituksiin tarkoitettu laitteisto koostuu pneumaattisesta iskutestauslaitteesta, jossa käytetään mekaanista iskua korkean G-arvon saavuttamiseen. Olemassa olevaa laitteistoa muutettiin siten että sillä voidaan saavuttaa suurempia G-arvoja (aina 80 000G:hen asti) ja mahdollistaa gyroskooppien tutkiminen eri asennoissa. Tärinäkuormituslaittesto koostuu signaaligeneraattorista ja täristinmoottorista, joka soveltuu gyroskooppien tärinätestaukseen. Signaaligeneraattoria käytetään eri taajuisten signaalimuotojen syöttämiseen täristinmoottorille, joka tärisee annetun syötteen mukaisesti.

Pyörityslaitteen toiminnallisuutta testattiin yhdellä gyroskoopilla huoneenlämmössä. Gyroskoopin X, Y ja Z-akselien kulmanopeuksien keskiarvot sekä -hajonta mitattiin. Korkean g-arvon iskutestauslaitteistoa testattiin kuudella mittauksella, jossa gyroskoopit rikkoutuivat ensimmäisellä iskulla. Tärinätestauslaitteistoa testattiin yhdellä gyroskooppi-piirilevyllä. Gyroskooppi-piirilevyn päälle asetettiin kiihtyvyysanturi, jolla mitattiin tärinästä aiheutuvan kiihtyvyyden RMS-arvo, huippuarvo ja kokonaisenergia. Tulevat jatkotutkimukset keskittyvät pyöritys-, isku- ja tärinälaitteistoilla testattujen MEMS-gyroskooppien vaurioanalyysiin.

Asiasanat: Gyroskooppi, MEMS, mekaaninen testaus, ympäristötestaus, luotettavuus, karakterisointi

Acknowledgements

This thesis was carried out in the Department of Electronics at Aalto University School of Science and Technology as a part of the MEMS (micro-electro mechanical systems) research project.

I would like to thank several people for being part of this project and helping me to finish my Master's Thesis: Docent Toni Mattila, for being the instructor of my thesis and head of the project team, for his advices and valuable guidance during this thesis. Professor Mervi Paulasto-Kröckel for being the supervisor of my thesis and providing me the opportunity to undertake my Master's Thesis on this interesting topic.

My sincere thanks go to the other close members of this project team: Mr. Jussi Hokka, for helping me with the test setups and making the printed wiring boards. Mr. Jue Li for his knowledge on mechanical aspects of reliability assessment. Mr. Matti Linnavuo for programming the test measurement software with LabView, and for his general ideas on automated testing. Former team member Mr. Henri Kari for designing board layouts and aiding with the CAM-program.

Special thanks go also to the technical support staff, especially Mr. Kimmo Rajala for his insight in mechanical design and assembly of the rotation test device, Mr. Heikki Ruotoistenmäki, Mrs. Pirjo Kontio and department secretarial staff for their help in many practical issues. I would also like to thank all the other people, especially Ms. Dong Hongqun, in the Electronics Integration and Reliability research unit for making a nice and enjoyable working atmosphere. In terms of funding and project support I would like to thank all the parties involved: Aalto University, Nokia, Okmetic, TEKES, VTI Technologies and VTT, for without this project would not have been possible.

All of my friends also deserve a thank you for all the good moments and memories. Finally, I would like to thank my parents, Markku and Arja, and my brother, Henrik, for their patience and support during my studies.

Thank you!

Espoo, August 9, 2011

Hannes Hyvönen

Contents

Abstract

Tiivistelmä i

Acknowledgements iii

Contents iv

Abbreviations and Acronyms v

1 Introduction 1

2 Operating Principles of Gyroscopes 3

2.1 Precession and Angular Momentum 3

2.2 The Coriolis Effect 5

3 Implementation of Gyroscopes 7

3.1 Vibrating Mass Gyroscopes 7

3.1.1 Tuning Fork Gyroscopes 8

3.1.2 Wine Glass Resonator 9

3.1.3 Vibrating Wheel Gyroscope 10

3.1.4 Piezoelectric Plate Gyroscope 11

3.1.5 Foucault Pendulum Gyroscope 11

3.1.6 Detection of Displacement in Vibrating Mass Gyroscopes 12

3.2 Optical Gyroscopes 15

3.2.1 Ring Laser Gyroscopes 15

3.2.2 Fiber Optical Gyroscopes 16

3.3 Typical Assembly Process of MEMS gyroscopes 17

4 Reliability Assessment of MEMS Gyroscopes under Harsh Conditions 20

4.1 High-G Shock Impact Tests 22

4.2 Vibration Tests 24

4.3 Environmental Testing 27

4.4 Gyroscope Performance Parameters 29

5 Research Question 31

6 Materials **32**
6.1 The Device under Test 32
6.1.1 Basic Structure of The Component 32
6.1.2 Sensing Element 33
6.1.3 Interface Integrated Circuit 33
6.1.4 Input and Output Pins 34
6.1.5 Gyroscope Communication Protocols 34
6.2 Printed Wiring Boards for Different Test Cases 37
6.2.1 Small Board for Evaluation of the Gyroscope 37
6.2.2 Large Board for Evaluation of the Gyroscope 38

7 Results of Characterization Development **40**
7.1 Results of Environmental Characterization 40
7.1.1 Environmental Characterization Equipment 40
7.1.2 Methods for Environmental Characterization 46
7.1.3 Testing of Environmental Characterization Equipment 48
7.2 Results of High-G Shock Impact Characterization 51
7.2.1 Shock Characterization Equipment 51
7.2.2 Methods for Shock Characterization 53
7.2.3 Testing of High-G Shock Impact Equipment 53
7.3 Results of Vibration Characterization 57
7.3.1 Vibration Characterization Equipment 57
7.3.2 Methods for Vibration Characterization 58
7.3.3 Testing of Vibration Equipment 59

8 Further Development **64**

9 Conclusions **65**

Appendix I **75**

Appendix II **76**

Appendix III **77**

Abbreviations and Acronyms

ASIC	Application Specific Integrated Circuit
CSA	Charge Sensitive Amplifiers
CSP	Chip Scale Package
DRIE	Deep Reactive Ion Etching
DUT	Device Under Test
EDP	Ethylenediamine-Pyrocatechol
FA	Failure Analysis
FEA	Finite Element Analysis
FIB	Focused Ion Beam
FOG	Fiber-Optic Gyroscope
HRG	Hemispherical Resonant Gyroscope
IC	Integrated Circuit
IR	Infra Red
I2C	Inter-Integrated Circuit Bus
LSB	Least Significant Bit
MEMS	Micro-Electro Mechanical System
MSB	Most Significant Bit
PCB	Printed Circuit Board
PEM	Photoelectron Microscopy
PSD	Power Spectral Density
PVC	Polyvinyl Chloride
PWB	Printed Wiring Board
PZT	Lead Zirconate Titanate
RF	Radio Frequency
RLG	Ring Laser Gyroscope
SAM	Scanning Acoustic Microscopy
SEM	Scanning Electron Microscopy
SOG	Silicon On Glass
SPI	Serial Peripheral Interface Bus
TEM	Transmission Electron Microscopy
TERO	Thickness Extension Resonance Oscillation
TIVA	Thermally Induced Voltage Alteration
TS	Thickness Shear Mode
USB	Universal Serial Bus
ZRO	Zero Output Velocity

1 Introduction

The market for micromechanical motion sensors is growing by rapidly over 50 million USD a year [1]. The consumers demand more intelligent devices that are aware of the environment they are in. Until today, the development of motion sensors has been driven by the needs of the automotive industry, but now a broader field of applications is available for the micro-electro-mechanical systems (MEMS) sensors. Consumer applications, specifically mobile phones and video games, appear to be very promising markets for MEMS motion sensors. Most common examples of MEMS motion sensors are accelerometers and gyroscopes. An accelerometer is an instrument used to measure acceleration, whereas a gyroscope is used to sense change in orientation and to measure angular velocity.

The physical operating principles behind gyroscopes are the conservation of angular momentum and the Coriolis effect. Historically, the angular rate has been measured with rotating wheel gyroscopes. Old, traditional gyroscopes, were usually a spinning disk or wheel of which the axle is free to adopt any orientation. In the present-day MEMS gyroscopes, the angular momentum is stored in a harmonic oscillator rather than a wheel. The present-day MEMS gyroscopes are lightweight, small, and relatively low-cost and, therefore, enable the utilization of gyroscopes in new applications that are not possible with the classic gyroscopes. Typical, but not limited applications for the present-day MEMS gyroscopes are related to gaming input devices or remote controllers, screen stabilization in digital cameras and inertial navigation when GPS signals are not available in mobile phones, for example.

The consumer MEMS gyroscope market is expected to reach 800 million USD in 2010 [1]. In 2003, there existed over 368 MEMS fabrication facilities worldwide, with strong centers in North America, Europe and Japan [2]. Several challenges include the increasing number of gyroscope manufacturers and changes in the value chain due to patents and supply issues. MEMS manufacturers are more and more willing to supply a whole sensor system instead of a bare sensor for a broad field of applications.

The field of MEMS gyroscope applications is considerably polarized. For example, in military and space applications, there is need for broader measurement bands and higher resolution, but for a simple application, such as sensing the orientation of a mobile phone, there is less need for higher resolution and keeping component costs down becomes more important. This is achievable by combining low-noise MEMS sensing elements with digital measurement electronics. The best MEMS sensing elements are implemented with reliable structures and packaging, which have been made possible with advances in sensing element design and manufacturing technology.

Reliability is defined as the probability that an item or a device will perform a required function under stated conditions for a stated period of time [3]. Reliability testing of MEMS devices is an essential part of the product development phase. The knowledge of making reliable MEMS gyroscopes is con-

sidered in this work by characterizing and testing a novel MEMS gyroscope. Extreme requirements for noise performance of the component and harshness of the operating conditions offer great challenges, not only for the component itself, but also for the requirements of test equipment performance.

This thesis presents a thermomechanical and mechanical assessment carried out on a novel microelectromechanical gyroscope. The mechanical assessment is performed by subjecting the gyroscopes to high-G shock impacts and vibrations. The thermomechanical assessment is performed through an environmental characterization of the gyroscopes in a thermal chamber. The first part of this thesis describes the general operating principles of gyroscopes and their implementation. A literature survey of a reliability assessment of MEMS gyroscopes, and similar MEMS devices, is also presented in the first part of this thesis. The second part of this thesis is the experimental part. The research question and the materials and methods used in this work refer to a 3-axial MEMS gyroscope and test equipment used to assess its reliability. To conclude this work, the developed equipment and methods for environmental, high-G shock impact and vibration testing, are presented. Failure modes are discussed briefly for high-G shock impact testing. Further development of the test equipment is discussed before final conclusions.

2 Operating Principles of Gyroscopes

A gyroscope is a device for measuring changes in orientation. Old, mechanical gyroscopes often resemble a spinning disk or wheel mounted on freely rotating joints or swivels. For example, if such a wheel is set into motion it remains nearly fixed when the gyroscope is turned around. This happens because a large angular momentum is stored in the rotating wheel based on the physical principle of the conservation of angular momentum. The freely rotating joints or swivels minimize the friction associated with the rotating wheel and it tends to maintain its orientation. In MEMS gyroscopes, the angular momentum is stored in a harmonic oscillator rather than a wheel.

MEMS gyroscopes use different implementations that are explained in Chapter 3. Common applications for gyroscopes include navigation when magnetic compasses are unusable (as in space telescopes) or are not precise enough or for the stabilization of flying vehicles, for example radio-controlled helicopters. Gyroscopes are used also to maintain direction, for example, in tunnel mining. [4, 5]

2.1 Precession and Angular Momentum

Mechanical gyroscopes date back to the 19th century in France, when a physicist named Jean-Bernard-Léon Foucault conducted experiments with the first spinning mass gyroscopes (Fig. 1) [6, 7, 8]. Etymology of the word "gyroscope" comes from Ancient Greek word "guros" meaning "circle" and "skopos" meaning "watcher" [5]. Foucault's experiments showed that a wheel or disk mounted so that it can spin freely around an axis that is itself free to assume any position maintains its direction despite the rotation of the Earth. This fact allowed the gyroscope, for example, to provide a reference direction in navigation systems. Also other application possibilities for the gyroscopes emerged such as autopilots and stabilizers in torpedos and ships [7, 6].

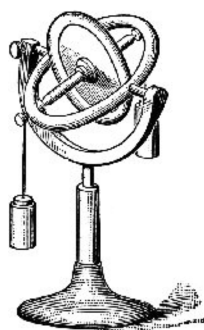

Figure 1: *Spinning mass gyroscope from the 19th century. Original image from [7].*

Looking back at the history of the gyroscopes, mechanical spinning mass gyroscopes were much smaller and precise in the 20th century than in the 19th

century. After spinning mass gyroscopes, laser-optical gyroscopes started to emerge in the 1960's and gained wide popularity in aeronautics and military applications [9]. First vibrating mass MEMS gyroscopes were introduced in the 1980s [10], and advancements have been made, in the last ten to fifteen years, to create smaller, more precise and mass-producible devices.

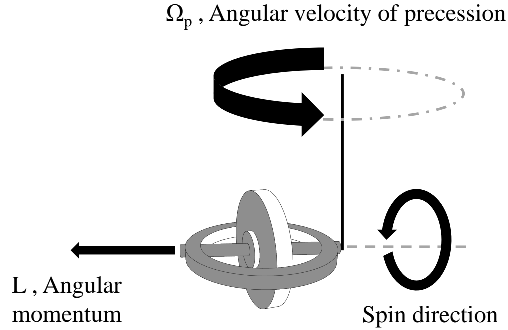

Figure 2: *Precession. Adapted from [7].*

Precession is the rotation of the axis of a spinning body around another axis due to forces (such as gravitation and equal support force) acting on the axis. Precession can be seen, for example, on a spinning top or a gyroscope. A spinning gyroscope that has its axis horizontal and loosely supported at one end does not fall, as might be intuitively expected, but keeps spinning as the free end of the axis begins rotating slowly (with angular velocity Ω_p) in a circle around the supporting point (Fig. 2). The gravitational and equal support force cause a torque that is directed around the precession axis. [4, 5, 7]

The direction of the torque, spin and precession vectors can be determined with the right hand rule. Forefinger (spin vector), middle finger (torque vector) and thumb (precession vector) are placed at a 90° degree angle to each other. For example, the spin vector can be imagined as an axis, around which the spinning motion takes place in a clockwise direction. The other two vectors (torque and precession) are perpendicular to the spin vector.

Motion of the gyroscope can be decribed by the fundamental equation:

$$\tau = \frac{dL}{dt} = \frac{d(I\Omega)}{dt} = I\alpha \tag{1}$$

where τ is torque, L is angular momentum, scalar I is moment of inertia, vector Ω is angular velocity and vector α is angular acceleration of the gyroscope.

Gravity of the gyroscope and distance from the support joint cause a torque that is perpendicular to the rotation axis. Torque τ can be calculated from:

$$\tau = r \times \Omega_p \tag{2}$$

where r is radius and Ω_p is angular velocity of precession. Under a constant torque of magnitude τ, the gyroscope's velocity of precession Ω_p is inversely proportional to L, the magnitude of its angular momentum:

$$\Omega_p = \frac{\tau}{L \sin(\theta)} \tag{3}$$

where θ is the angle between vectors Ω_p and L. Friction can cause the gyroscope's spin to slow down and make the angular momentum of the gyroscope decrease. Therefore, as described by Equation 3, the velocity of precession increases as the angular momentum decreases. The gyroscope's spin slows down gradually so it cannot support its own weight. Eventually, the gyroscope will stop precessing and fall off its support. [7, 5]

2.2 The Coriolis Effect

The Coriolis effect is a physical phenomenon that affects a mass moving in a rotating system. The mass in a rotating system experiences a force (the Coriolis force) that acts perpendicular to the axis of the rotation of the system and to the direction where the mass is moving. The Coriolis effect is caused by the rotation of the Earth and the inertia of the mass under the effect. In the rotating system, when it is rotating clockwise, the Coriolis force tends to deflect moving objects to the left. In counter-clockwise rotation the direction of deflection is to the right. The motion of an object in a rotating system can be described by the Coriolis and the centrifugal forces. Both of which depend on the mass of the object.

The Coriolis force can be described by the formula:

$$F_c = ma_c \tag{4}$$

where F_c is the Coriolis force, m is the mass of the object, a_c is the Coriolis acceleration that can be calculated with the formula:

$$a_c = 2v \times \Omega_p \tag{5}$$

where v is the linear velocity of the moving object in relation to the rotating frame of reference and Ω_p is the angular velocity.

If we attach the moving mass (Fig. 3) to a stable structure with spring constant k, we get the deflection x of the mass from equation:

$$x = \frac{F_c}{k} = \frac{ma_c}{k} = \frac{a_c}{(2\pi f)^2} \tag{6}$$

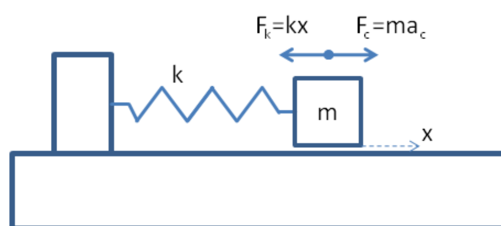

Figure 3: *Moving mass attached to a stable structure with a spring. The mass is affected by Coriolis force and equal spring force. This situation is similar to the function of vibrating MEMS gyroscopes.*

where f is the resonance frequency. For example, vibrating MEMS gyroscopes are based on the equation above and are explained more thoroughly in the next chapter (Chapter 3).

3 Implementation of Gyroscopes

In this chapter, in addition to the spinning mass gyroscope presented in earlier chapter, two different implementation types of gyroscopes are presented: vibrating mass and optical. Vibrating mass gyroscopes are the most common MEMS gyroscopes. They are based on the Coriolis effect and vibrating structures. Optical gyroscopes are based on the measurement of time differences in laser paths, they are very expensive but also provide good accuracy. The typical assembly process of MEMS gyroscopes is also presented at the end of this Chapter to gain a better understanding of how MEMS gyroscope structures are usually manufactured.

3.1 Vibrating Mass Gyroscopes

The vibrating mass gyroscopes rely on the Coriolis effect and the coupling of energy between two modes of vibration for sensing angular velocity. The primary mode of vibration is called the drive-mode that sets the mass to vibrate in a linear direction. This is usually done electrostatically. The secondary mode of vibration is called the sense-mode. The Coriolis effect induces the secondary vibration because of the combination of drive-mode vibration and an external angular velocity input. The displacement of gyroscope inner structures caused by the sense-mode vibration can be sensed, for example, capacitively or piezoelectrically. This displacement is linked to the angular velocity. Primary mode and secondary mode are pictured in Figure 4. [8, 11, 12]

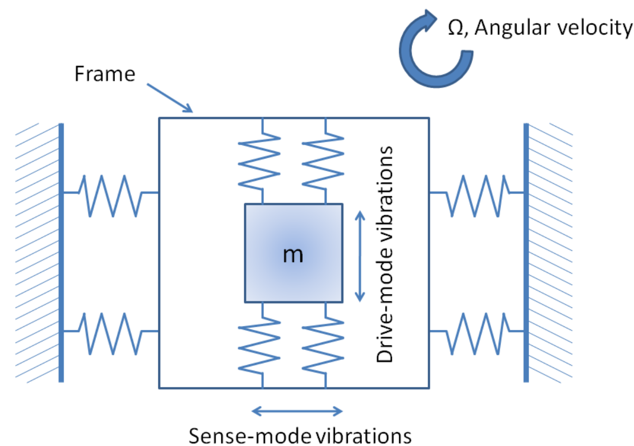

Figure 4: *Two modes of vibrating mass gyroscopes. Primary (drive) and secondary (sense) modes.*

3.1.1 Tuning Fork Gyroscopes

The tuning fork gyroscope was first proposed by Draper Lab in 1986 [10]. It resembles a tuning fork in structure and function (Fig. 5) and is very common in vibrating mass gyroscopes. It is made from a dual proof masses which are connected with beam and comb structures to each other. The dual proof masses are then actuated to vibration in opposite directions but with the same amplitude of vibration [13, 14, 15]. The vibrating masses experience a Coriolis force when under external angular velocity, and this force causes displacement in the comb structures and can be measured with sense electrodes.

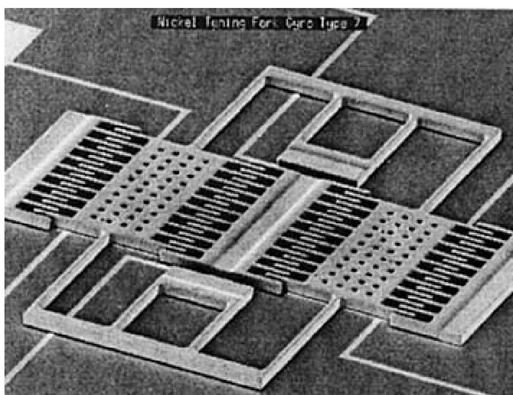

Figure 5: *Draper Lab gyroscope. Original image from [11].*

Comb structures are very common in tuning fork gyroscopes (Fig. 6). The combs are used to drive the tuning fork into vibration but also to sense the displacement capacitively [8, 14, 16]. Detection of displacement in vibrating mass gyroscopes is further discussed in Chapter 3.1.6.

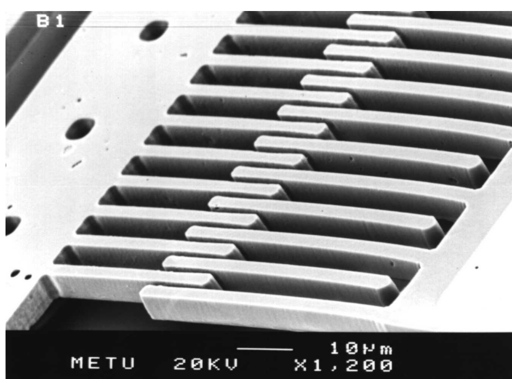

Figure 6: *Typical MEMS comb structures. Original image from [17].*

3.1.2 Wine Glass Resonator

The wine glass gyroscope is another type of vibrating mass gyroscope. It is named by its shape that resembles a wine glass. It is also known as the hemispherical resonant gyroscope (HRG) [14, 18]. The HRG's sensitive element design is usually based on a hemispheric resonating shell (Fig. 7). Basic structure of the HRG consists of a resonating shell, an actuator to resonate the structure and pick-off electrode and capacitor system to measure output in the resonating shell [19, 18, 20, 21].

Figure 7: *Different hemispherical resonant gyroscopes, also known as wine glass gyroscope, designs. Original images from [21].*

A standing wave can be actuated in the rim of the hemispherical resonator shell by a voltage applied to an actuator. The nodes of the standing wave are stationary when there is no external angular velocity present. The standing wave can change its location on the resonator shell, due to the Coriolis effect, when the gyroscope is rotating. The standing wave rotates with respect to the shell through an angle that is approximately 0.3 times the external angular velocity rotation angle [21, 20, 22]. The location of the standing wave can be estimated with electrodes placed around the shell of the rim [21, 18]. The design of the HRG is very similar to the thin micromechanical cylinder or ring, and sometimes these names are used interchangeably with the wine glass resonator [11, 23].

The HRG accuracy is affected by the possible energy losses in the actuator, pick-off electrodes and capacitor systems. The main way of increasing the HRG accuracy is to minimize these energy losses. Because of different manufacturing processes and materials and operating conditions the HRG is subjected to noise environments. These noise effects can be compensated with, for example, wavelet or similar filtering [24, 25, 26], different readout loops [19, 20, 27] and providing minimum possible damping [22, 20, 28].

To retain potentially high characteristics of the material in a manufactured resonator one must minimize internal stress and defective layers from the resonator material. Criterion of resonator quality is often expressed as the Q factor (Q for quality). The Q factor is a dimensionless parameter that describes how under-damped an oscillator or resonator is. A higher Q factor

indicates a lower rate of energy loss relative to the stored energy of the oscillator, and hence oscillations die out more slowly. Oscillators with high quality factors have low damping so that they ring longer.

In summary, to implement hemispherical resonator gyroscope's potential capabilities one should solve a number of challenges in manufacturing an isotropic resonator having a high Q factor. The resonator should also combine an electrostatic system for excitation, support and control of vibrations on a resonance frequency.

3.1.3 Vibrating Wheel Gyroscope

Vibrating wheel gyroscope's structure resembles a wheel or a ring. Vibrating wheel gyroscope is driven to vibrate around its center axis, and when it changes its orientation due to Coriolis force, this change (with respect to angular velocity) can be measured, for example, capacitively [29, 30, 31, 32, 33]. Therefore, it is sometimes called the plate gyroscope because of possible plate capacitive electrodes under or at the rim of the wheel [14, 32]. One typical design of the vibrating wheel gyroscope is presented in Figure 8.

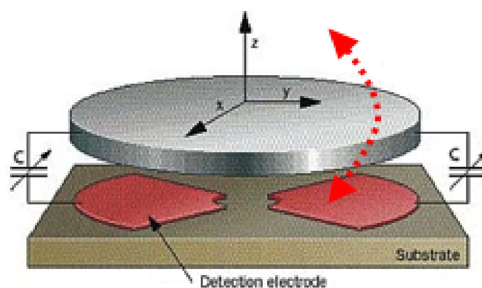

Figure 8: *Illustration of a vibrating wheel gyroscope also known as plate gyroscope. Tilting direction of the gyroscope marked with the red arrow. Image adapted from [11].*

It can be said that the vibrating wheel and the tuning fork design are very similar, both are approximately the same size and use a larger proof mass to provide the coupling for the Coriolis force to measure angular velocity [32, 33, 31]. The proof mass of the vibrating wheel is commonly made out of surface-micromachined polysilicon. The mechanical resonator, sense and drive electronics could be combined on a single chip for more efficient miniturization [32, 14]. Usually they are separate, with static electrode-combs on a surface to drive the wheel in motion, and sensing is done with capacitance pickoff electrodes under the wheel [29, 30, 33]. There has been considerable advancements in the MEMS fabrication techniques, for example, in the 1980s, the size was restricted to about two microns of structural polysilicon [11]. However, modern MEMS gyroscope process technologies are capable of producing structures as thin as 0,35 microns or even 0,18 microns [34, 13].

3.1.4 Piezoelectric Plate Gyroscope

Piezoelectric materials can be used to make modern MEMS gyroscopes [12, 35, 36, 37, 38, 39, 40, 41]. Piezoelectricity is a linking between material's mechanical and electrical properties. In the simplest way, when a piezoelectric material is bent or compressed, an electric charge collects on its surface and this charge (voltage) can be measured. For example, Hong Kong University of Science and Technology conducted a study of a piezoelectric plate gyroscope (Fig. 9) [42]. The piezoelectric plate is made of a lead zirconate titanate (PZT) film. PZT is a ceramic material that develops a voltage difference between two of its faces when compressed. This is called the piezoelectric effect [4, 42].

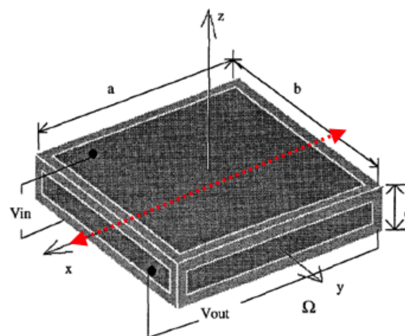

Figure 9: *Illustration of a piezoelectric-plate microgyroscope, where a, b, and c are the length, width and height of the piezoelectric plate. Thickness resonance oscillation direction marked with the red arrow. Image adapted from [42].*

The polarization direction of the PZT film is in the z-axis. The piezoelectric plate is excited (voltage V_{in}) in the polarization direction (z-axis) to produce thickness extension resonance oscillation (TERO). There also exist some references that relate to thickness shear mode (TS) [35, 38, 41, 36, 40], but both modes are very much alike. Thickness extension resonance oscillation makes the piezoelectric material to extend and oscillate in the x-direction, which can be measured as a change in voltage (V_{out}). This oscillation is coupled by the Coriolis effect and allows a single chip to sense two axes of rotation [42, 36, 41].

3.1.5 Foucault Pendulum Gyroscope

The Foucault pendulum gyroscope consists of a vibrating rod, beam or other large mass that is oriented out of the plane of the gyroscope chip [11, 43, 44, 45]. It is named after the famous physisict Jean Foucault (presented in Chap. 2). He made observations of the Coriolis effect with a device called the Foucault pendulum. The Foucault pendulum is a swinging pendulum that is attached to a rotating frame of reference (i.e. Earth) and set to

motion. Eventually, the pendulum starts to move in a precession motion that is related to Earth's rotation and the Coriolis effect [8, 4].

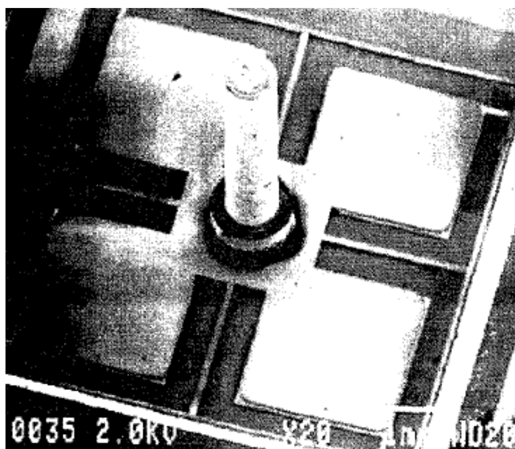

Figure 10: *SEM picture of a Foucault pendulum gyroscope. Vibrating rod oriented out of the plane of the chip. Original image from [45].*

Figure 10 presents a silicon micromachined gyroscope that resembles a four leaf clover that has a relatively large metal post attached to its center. The large surface area of the clover leaf electrodes is suitable for electrostatic drive and sensing at the lowest resonance frequencies. The metal post is made to provide a strong Coriolis force coupling between the drive and sense modes when the gyroscope rotates around the center post axis. [43, 44, 45, 46]

Large mass at the center of the symmetric four leaf clover stucture makes the whole gyroscope easier to balance and also increases the Q factor [43, 44, 45]. Higher Q factor of the resonator can increase the sensitivity of the gyroscope, but at the cost of possibly increasing the gain difference required to start and maintain resonance. High gain levels during startup of resonance can lead to uncontrollable high frequency electrical oscillations. Therefore, gain of the voltage controlled amplifier should be adjustable to reduce the gain level at frequencies above resonance. [44, 45]

3.1.6 Detection of Displacement in Vibrating Mass Gyroscopes

There are multiple ways of detecting the displacement of the proof mass. The detection can be capacitive, magnetic, optical, piezoelectric and piezoresistive, for example [8, 47, 48, 49]. Piezoresistivity, one of the most common detection methods, is the changing resistivity of material due to mechanical stress. In piezoresistivity the material's resistance changes and the material does not produce elecric charge on its surface, contrary to piezoelectricity.

Capacitive detection of displacement uses comb-like capacitive structures (Fig. 11). The capacitance between the movable mass and the fixed electrodes can be estimated as a parallel plate capacitor where the capacitance is given by

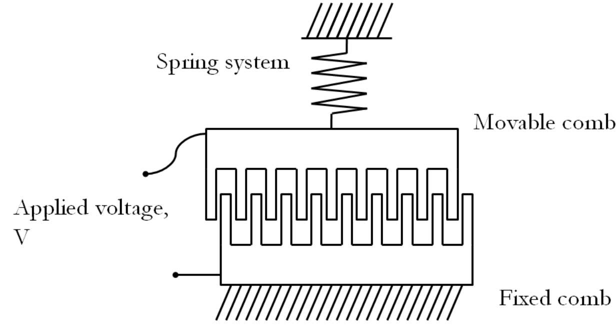

Figure 11: *Comb-drive capacitive structure.*

$$C = \frac{\epsilon A}{d} \tag{7}$$

where ϵ is the electrical permittivity, A is the overlapping area between two comb electrodes, and d is the distance between the two comb electrodes that act as two parallel plate capacitors. As the proof mass moves between the fixed comb electrode, the capacitance between the comb electrode and moving electrode changes. This capacitance change can be modeled by

$$\frac{\partial \Delta C}{\partial x} \approx \frac{2\epsilon A}{d^2} \tag{8}$$

where $\Delta C = C_1 - C_2$ and a linearized model has been assumed so that $d_1 = d_2 = d$, and x is the displacement of the element.

From equation 8 we can write

$$\Delta C \sim K \Delta x \tag{9}$$

where constant $K = \frac{2A\epsilon}{d^2}$, and the change of capacitance is directly proportional to the displacement.

Piezoresistive detection is analogous to capacitive detection. Measurement of resistivity is used instead of measurement of capacitance. When piezoresistive material bends or is otherwise deformed, the resistivity of the material changes, and this change is proportional to the displacement. The piezoresistive detection has some benefits over capacitive detection: piezoresistive sensors are simpler to make than dense comb-structures and the lower impedance makes the signal output larger and therefore easier to detect [50, 51].

However, piezoresitive detection has two drawbacks compared to capacitive detection. The first drawback is the high temperature dependence of piezoresistive materials that causes temperature drift in the measured angular velocity signals [50, 51]. The second drawback is the need to improve the sensitivity of piezoresistive detection. As the Coriolis effect is a rather weak effect the sensitivity of the detection should be kept high. Typical piezoresistive detection utilizing a bending beam can have a relatively low sensitivity

[51], because of the possible bending stress in the beam can be very scattered [52, 53]. On the other hand, these effects could be compensated, for example, with suitable control phase-loops and a careful choice and treatment of piezoresistive materials [53, 54].

In summary, only a small part of Coriolis effect induced stress is translated into piezoresistively detectable signal, which causes low sensitivity. Improvement of sensitivity can result in a decrease in resonant frequency, this means that the low frequency operation of vibratory gyroscope can be affected by environmental mechanical vibration [51, 53, 54]. Environmental mechanical vibration is usually under 1kHz, but when it is near the gyroscope resonance frequency, it should be somehow avoided entirely or compensated effectively.

The displacement in primary vibration motion is x, and k is the spring constant of a beam structure. Now, recalling the Coriolis force $a_c = 2\Omega v$ the secondary sense motion caused by rotation can be written as [48]

$$y = \frac{ma_c}{k} = \frac{m(2\Omega v)}{k} = \frac{2m\Omega xt}{k} \tag{10}$$

This equation demonstrates that the amplitude of secondary oscillation (y) is directly proportional to the angular rate (Ω) signal to be measured.

3.2 Optical Gyroscopes

Optical gyroscopes are a great advancement to the spinning mass gyroscopes in that there is no mechanical wear because of missing gimbal or spinning mass structures. This also makes them smaller in size and weight than classical spinning mass gyroscopes, but not nearly as small and compact as MEMS gyroscopes. However, due to advancements in modern optics, manufacturing of optical MEMS gyroscopes might be possible in the near future.

The first optical gyroscopes were ring laser gyroscopes (RLGs) [55, 7]. These devices accelerate two lasers around a circular path in opposite directions. A phase shift can be detected if the path spins, since the speed of light remains constant. Customarily the rings are rectangles or triangles with mirrors at each corner.

Another type of optical gyroscope is the fibre-optic gyroscope (FOG), in which light is routed through thin optic fibers that enclose a circle [7, 56]. Therefore, it does not use hollow tubes or mirrors that might easily be bulky and take up too much space, becoming somewhat impractical.

The operating principle behind optical gyroscopes is the Sagnac effect [7, 57]. It is sometimes also known as the Sagnac interference, and it is named after French physisict Georges Sagnac. In the Sagnac effect a beam of light is split and the two separate beams are made to follow a path in opposite directions (clockwise and counter-clockwise). The path of the light beams must encloce an area that is usually a circle. Light is allowed to exit the device in such a way that an interference pattern is obtained. The Sagnac effect causes a time difference between the two opposite traveling light beams and the time difference can be calculated with the following equation [7]

$$\Delta t = \frac{4\pi R^2 \Omega_{rot}}{c^2} = \frac{4A\Omega_{rot}}{c^2} \tag{11}$$

where A is the area of the ring, Ω_{rot} is the angular velocity of the rotating ring (where the light travels) and c is the speed of light. This equation depicts that the time difference, and the position of the interference pattern, is dependent on the angular velocity of the device (optical gyroscope).

3.2.1 Ring Laser Gyroscopes

The ring laser gyroscope (RLG) has a ring path with mirrors and inside the ring path there are two counter-propagating laser beams (Fig. 12). The laser beams travel in opposite directions and interferere to produce a interference pattern. The rotation of the RLG is causing the Sagnac effect to shift the nodes of the interference pattern so that there is a time difference between the two counter-propagating laser beams. [7, 58, 59]

The benefit of using an RLG is that there are no moving parts. Although RLGs are more accurate than mechanical gyroscopes they suffer from a phe-

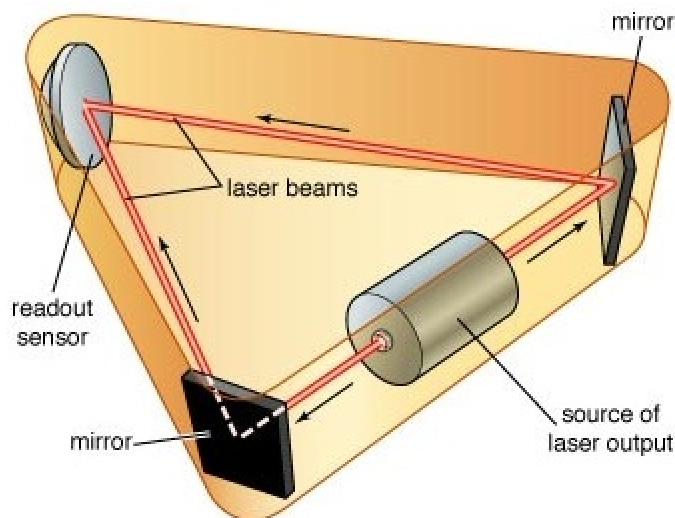

Figure 12: *Ring laser gyroscope illustration. Original image from [7].*

nomenon known as lock-in [55, 59, 9] at considerably slow rotation rates. The frequencies of the opposite traversing laser beams become almost identical, when the RLG is barely rotating. In this situation, the crosstalk between beams can permit lock-in so that the standing wave gets stuck in a preferred phase and locks the frequency of both beams. Lock-in then causes the angular velocity corresponding to rotation difficult or even impossible to measure, because there is no frequency or time-difference between the two beams any more.

3.2.2 Fiber Optical Gyroscopes

A fibre optic gyroscope (FOG, Fig. 13), like the RLG, uses the interference of light (especially the Sagnac effect) to detect mechanical rotation. The first fiber optic gyroscopes were developed due to the advancements in low loss single mode optical fibers for the telecommunications industry in the early 1970s [60]. Compared to RLGs, FOGs use optic fibers as path for light beams rather than mirrors. This makes them more compact than RLGs.

An FOG accommodates highly precise rotational rate information. Because it lacks cross-axis sensitivity to acceleration, vibration, and shock [61, 60]. Optical gyroscopes have virtually no moving parts and no inertial resistance to movement. Therefore, FOG technology is considered to be one of the most reliable gyroscope technologies and allows for their use in high performance applications.

The FOG commonly displays a higher resolution than an RLG but used to have less stable zero rate output (also known as bias) until the end of the 90s. Zero rate output (ZRO) is the average over a specified time of gyroscope output measured at specified operating conditions that has no correlation with input rotation. ZRO is typically expressed in $°/sec$ or $°/hr$.

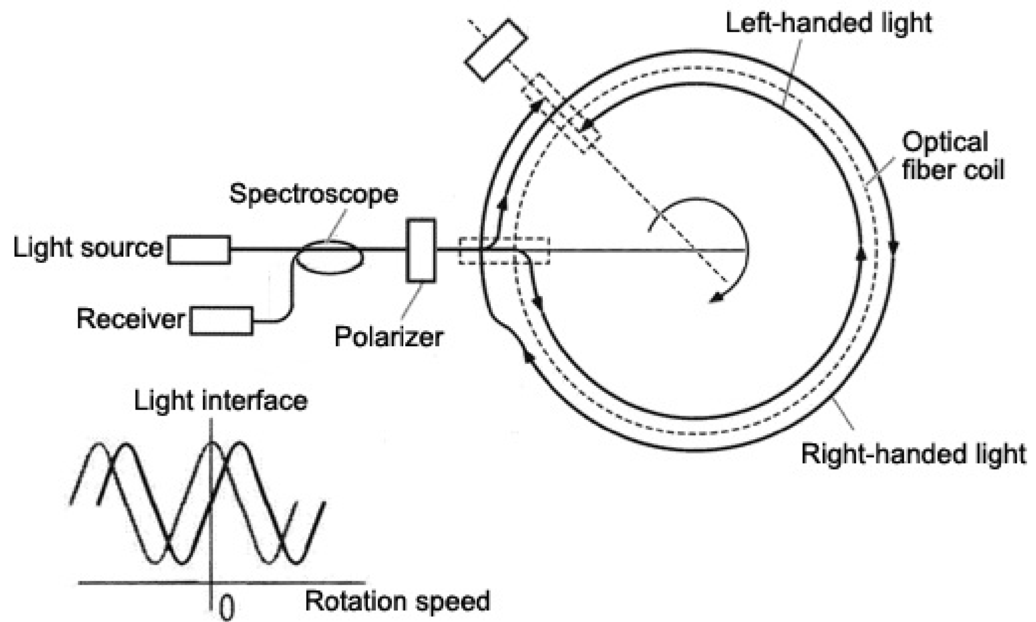

Figure 13: *Fiber optical gyroscope principle. Original image from [61]*

High-performance FOGs have showed better ZRO stability than the most accurate RLGs. [56]

As there is very little research available on optical MEMS gyroscopes, further discussion on optical gyroscopes is considered to be beyond the scope of this thesis.

3.3 Typical Assembly Process of MEMS gyroscopes

Micromechanical gyroscopes have both bulk- and surface micro-machined structures. Bulk micro-machined structures have a relatively larger size and mass compared to surface micro-machined structures. Most bulk micro-machined gyroscopes do not have control electronics (such as ASIC) integrated in the same chip. In bulk micro-machined gyroscopes, the control electronics are usually in separate chips connected by wire bonding or with other wiring to the gyroscope. This two-chip-solution requires larger packaging size and limits its use in some applications. Surface micro-machined structures on the other hand have smaller mass and size than bulk micro-machined structures. This has made it possible to integrate the gyroscope and the control electronics on the same chip, which reduces fabrication and packaging costs considerably. [62, 63]

The typical fabrication process is depicted in Figure 14. The fabrication process pictured for a MEMS gyroscope is a silicon on glass process (SOG) that means bonding silicon wafer on a glass surface. The fabrication process is a very simple three mask process. It is based on the dissolved wafer process combined with the deep reactive ion etching (DRIE). The first process step

is the deep-boron diffusion of a silicon wafer to a high doping density. Then, a DRIE etch is performed from the boron doped front side of the silicon wafer to form the gyroscope patterns. The silicon wafer is then flipped and anodically bonded to a glass wafer. The last part is dissolving of the undoped silicon wafer in an ethylenediamine-pyrocatechol (EDP) solution. This leaves the boron-doped single-crystal silicon structures on the glass substrate and forms the gyroscopes. [64]

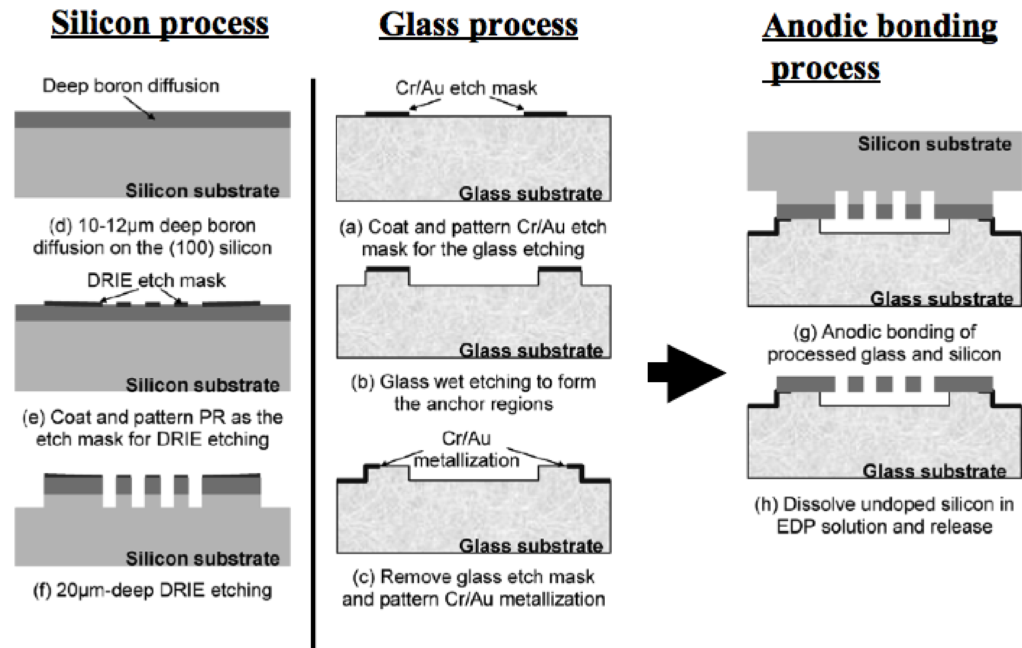

Figure 14: *Typical silicon on glass (SOG) fabrication process for a MEMS gyroscope. Image adapted from [64].*

Silicon is the typical building material of MEMS devices. It is naturally a semiconductor, and an easy material to process with. Depending on the doping materials used, silicon can work either as an insulator or a conductor. It has a drawback of being quite a brittle material. Different processing conditions can make the mechanical properties and defects of silicon vary significantly. Small changes in the pressure, deposition temperature and gas flow rates can add the number of point defects, dislocations and thermal mismatches for deposited thin films [65]. Irregularity in the manufacturing process can directly affect the failure modes and consecutively the reliability of MEMS structures.

It is important to understand the basics of different assembly processes to gain a better understanding of reliability issues related to manufacturing. The emphasis of techniques moving from research to industrial manufacturing increases also the importance of the costs related to the capital cost of equipment and of device manufacture. For example, the costs of packaging can be creater than 50% of the device costs, even utilizing standard semi-

conductor packaging [66]. The manufacturing process may not always be the best in terms of reliability, but is more a trade-off between costs and reliability.

4 Reliability Assessment of MEMS Gyroscopes under Harsh Conditions

Microelectromechanical devices are often designed to work in harsh conditions arising from the environment. Harsh conditions include for example:

- high temperature,
- high pressure,
- high humidity,
- corrosive gases or liquids,
- dust,
- high power density,
- mechanical shocks and vibration,
- intensity of magnetic and electrical fields,
- radiation, and many others.

These harsh conditions can make MEMS devices considerably prone to reliability issues. Applications of MEMS devices for military, medical and space environments are progressively increasing. Therefore, it is essential to focus on the reliability expertise and testing of MEMS components. Reliability testing of MEMS components in harsh environments calls for standardized tests. There is a need for accelerated tests in different temperature and corrosive environments. Such as accelerated tests using device storage temperature, or functionality testing at elevated temperatures. Reliability assessment of MEMS devices in harsh conditions is arguably going to be a cutting edge area where research labs are starting to elaborate new testing concepts.

Realizing the novel nature of testing concepts, a collaborative approach is needed to deal with the vast task of reliability engineering of MEMS devices. The test methodology, physics of failure, packaging, as well as computer simulations and modeling need to be considered. There exist a large list of possible reliability and failure mechanism issues that can be seen in MEMS devices. Problems in packaging due to miniaturization and heat transfer can be considered universal for all MEMS devices [67]. There are also many specific failure modes that are more common in one type of MEMS device than the other. One special failure mode is for example stiction [68] ("static friction" of two surfaces together) found in MEMS gyroscopes or microphones (Fig. 15).

Other common failure mechanisms include: failure by wear, delamination, environmentally induced failures and fatigue. Wear is the gradual deterioration of mechanical parts which results naturally from use. Delamination

is the failure by separation or loss of adhesion between two different layers. Some of the environmentally induced failures are common for all electrical devices, such as corrosion, internal currents and heat issues. In addition to these environmentally induced failures there are inner failure types that are encountered in MEMS structures and are much more difficult to examine, such as stiction. [69, 70]

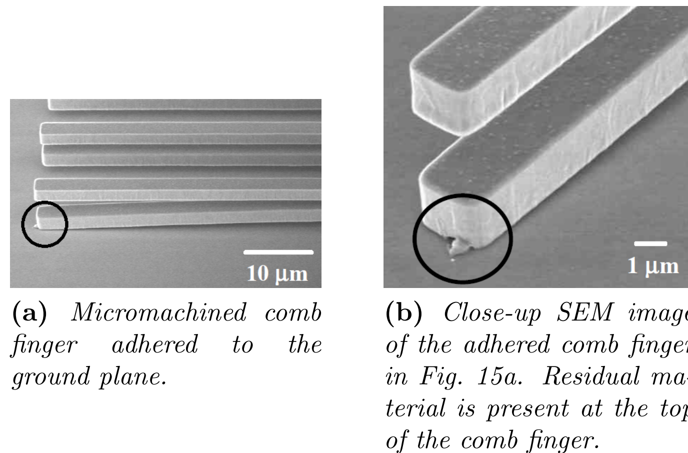

(a) *Micromachined comb finger adhered to the ground plane.*

(b) *Close-up SEM image of the adhered comb finger in Fig. 15a. Residual material is present at the top of the comb finger.*

Figure 15: *Stiction of comb finger to the ground plane. There also exists stiction between comb fingers. Original images from [71].*

Failure analysis of MEMS components requires careful inspection to understand the root causes of failure. Failure analysis can be performed at the wafer and die level with little or no sample preparation, but after fabrication it is not so straightforward. The device can be packaged, capped, hermetically sealed, or otherwise blocked requiring usually disturbing the device or its immediate environment [72].

It can be concluded that MEMS have very specific failure modes. Several failure analysis (FA) techniques that are conventionally used for FA of chips and packages, can also be used for MEMS. Especially useful are SEM (scanning electron microscopy) for inspection, and FIB (focused ion beam) to make local cross-sections. Techniques such as transmission electron microscopy (TEM), photoelectron microscopy (PEM), scanning acoustic microscopy (SAM), infra red microscopy (IR), X-ray and even thermally induced voltage alteration (TIVA) find applications in MEMS failure analysis. [73]

This chapter (Chapter 4) is based on a literature survey on the characterization of different MEMS devices carried out by different universities and research groups. This chapter is divided into three parts: high-G impact tests, vibration tests and environmental testing. There is a brief summary at the end of each part of the most relevant findings. Gyroscope performance parameters are discussed separately in Chapter 4.4.

4.1 High-G Shock Impact Tests

One of the toughest demands is the ability of a packaged sensor to survive a drop-test. However, since the mass of the structures is tiny, the devices can be quite resistant to shock and vibration [74]. The typical height for drop tests is between 1 and 1.5 m, which has shown to lead to accelerations in the range of 10 000G to 100 000G [74]. The G-value means the value of acceleration due to gravity so +1G equals approximately an acceleration of 9.82 m/s^2. There exist various damage types caused by impact shocks. Shocks can induce cracks in the material which can cause fractures. Shocks may also chip away small pieces of material which may, for example, cause short-circuits or block moving structures in sensors.

Drop-tests are defined by the acceleration pulse (G-value of the shock), drop-heights and test object orientations [75] used. Also the surface conditions of the contacting surface affect the force of the impact, for example dampening the shock [76]. There exists standards for board-level drop tests, standardized by the Joint Operation Electronic Devices Engineering Council (JEDEC) [77, 78]. It is useful to apply these board-level standards, when making drop-tests for MEMS devices to gain also knowledge of boundary conditions in the package level [79]. These boundary conditions can also be applied for simulations and measurements to help design better tests for board-level testing.

The exposure of MEMS devices and components to shock environments can occur during assembly, fabrication or operation. Shocks induced by accidental drops onto hard surfaces are a significant reliability concern. Similarly, MEMS used in space applications and those used to monitor intense impact environments will experience dynamic loading during deployment and operation [80]. Designing stable structures under dynamic load bids awareness of

- the stress history of the structures during the impact,
- a theory explaining the severity of the load experienced by the structure, and
- the appropriate material properties.

The stress history and distribution can often be modeled, for example, by applying dynamic finite element analysis (FEA) (Fig. 16) methods [82]. **In a simulation study by Weber et. al (2004)**, the effects of high operating accelerations (up to 500 G's) were observed with simulation software for a sample MEMS gyroscope structure [83]. Displacement of the proof mass and other shock effects were simulated. Gyroscopes exposed to high-G environments will likely have some type of isolator between the gyroscope housing and the sensor elements. The shock effects were simulated with and without an isolator placed between the gyroscope housing and the sensor elements [83].

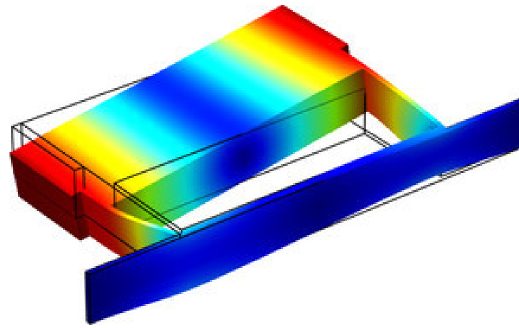

Figure 16: *Illustration of a typical finite element analysis (FEA) model. Original image [81].*

Simulation study [83] findings were: without an isolator the simulation software determined the gyroscope's proof mass displacement to be $6\mu m$ when exposed to a 500G shock. The amplitude of the shock was dampened by more than a factor of 20 with an isolator. A critical displacement value can be derived from the displacement values. It is the boundary value between a safe operation region and a snap-down region. Snap-down is the failure that occurs when the electrostatic forces between a proof mass and a comb-electrode become too large. In a snap-down situation the proof mass touches the comb-electrode sense plates and the gyroscope has "snapped-down" resulting in short-circuit or stiction. **In summary,** there is a minimum sense gap to prevent snap-down that should be determined for each gyroscope design. It is also advisable to place an isolator between the gyroscope housing and the sensor element to dampen the amplitude of shock impacts. [83]

Srikar and Senturia (2002) conducted shock tests on packaged surface-micromachined devices [80]. Mechanical responses of a large class of shock loaded MEMS were modeled as microstructures attached to elastic substrates. The shock reliability of many MEMS devices has been studied experimentally. In a small subset of these studies, the response of the microstructures has been monitored during the shock excitation. The intensity of the shock ranged from 20G to 120 000G, and the shock durations varied from 40 to $3000\mu s$. **Several conclusions were made about the failure criteria and responses to shock load of MEMS structures in this study.** MEMS attached to a substrate can be modeled as undamped resonators attached to an accelerating support. Shocks with durations less than $50\mu s$ make the substrate where the microstructures are attached respond as a rigid body that is expected to be immune to stress-wave-induced damage. Failure criteria can be formulated either in terms of a critical stress or a critical displacement.

The U.S. Army Research Laboratory has conducted a series of research about MEMS devices under harsh military environments [84, 85]. **In the reference [84]**, devices were subjected to severe high-G shock environments of up to 35 000G. High-G testing consisted of both short (shock table) and long-pulse

(air-gun) duration shocks. A simple drop-test machine was used to perform the initial experiments. Simulated shocks were less than 1ms in duration and had a higher rebound effect as compared to real (missile or cannon) launch conditions. Survivability at missile launch conditions and laboratory experiments is different in some ways. High frequency content and magnitude of the shock impact can be said to be more harsh in laboratory conditions than during launch conditions.

Results in [84] can be concluded as follows: Differences between the high-G shock impact loading on the shock table and within the test sample were larger without a damping material. During a 20 000G shock the measured shock within the test sample was as large as 75 000G. Only 30 000G was measured in the test sample with damping material during a shock of the same magnitude (20 000G). Understanding the dynamics of loading on specimens is critical in order to build a better dynamical model and take account the various damping materials that can be used to lessen the shock impact effects.

Overall findings in this literature survey of high-G impact tests for MEMS devices can be summarised as follows:

- MEMS devices have been tested from as low as 20g's up to as high as 120 000g's.
- Shock duration has varied from 40 to 3000μs. With durations over 50μs the MEMS substrate has shown response as a rigid body.
- Damping material placed between a mounting surface of a sample can more than halve the shock impact loading within a MEMS device in a drop test.
- Failure criteria of the MEMS devices can be formulated for example with critical stress or critical displacement parameters.
- There are JEDEC standards for board-level drop tests, but none especially designed for MEMS gyroscopes. However, many gyroscope manufacturers promise some exact level of shock impact survivability in specific G-values, although the conditions are often incomparable between different gyroscopes.

4.2 Vibration Tests

Besides impacts and shocks, MEMS gyroscopes can also be subject to vibrations. Vibrations can cause high alternating stresses that produce fatigue failure in MEMS gyroscopes. There are many sources of structural and mechanical vibration that the engineer must take account of when designing complex engineering systems: motion, usually rotation, induced by machinery; ground-borne propagation due to construction; vibration from heavy

vehicles as well as vibratory propagation from rail systems; and vibrations included by natural phenomena, such as wind or earthquakes.

Vibrations are often modeled as periodic and sinusoid functions, but in real life the sources of vibration are hardly periodic. These include impulsive forces and shock loading, random excitations and aperiodic motions. Therefore, it is reasonable to make assumptions about the resonant frequency and a single set of parameters to describe the mass, the stiffness and the damping of MEMS gyroscope structures.

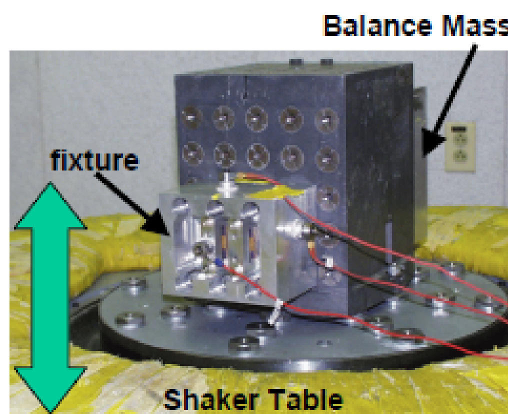

Figure 17: *Typical vibration environment, shaker table. Arrows indicate direction of vibration. Original image from [71].*

Vibration test are usually performed in an environment that has certain peak amplitude, acceleration and spans certain frequencies. Also different modes of vibration and duration time can be altered. It is sensible to test functionality of the gyroscopes before and after the test rather than during the test, because the operating principle of the most gyroscopes is based on vibration and energy stored in a harmonic oscillator. Under constant vibration, gyroscopes would output arbitrary angular information. Nonetheless, it is important that they work reliably afterwards.

In a vibration study by Choa (2002), gyroscope chips were subject to a vibration that had a acceleration of 9G, peak amplitude of 1.5mm and spanned frequencies from 15 to 55Hz. Test duration was 40 minutes and three modes of vibration were used. No performance changes were observed following this vibration test. **In this study, it could be concluded** that the device under test (DUT) was robust enough to pass a typical vibration qualification test for electronic products. [74]

Tanner et al. (2000) performed a vibration test to surface-micromachined microengines and observed the failures in them. The test was carried out in a vibration environment (Fig. 17) that had a peak acceleration of 120G and spanned frequencies from 20 to 2000Hz. The surface-micromachined microengines contained many elements (springs, gears, abrasive surfaces) sensitive to vibration. [71]

Relevant findings in [71] were: two vibration related failures and three electrical failures in a set of 22 microengines. Failure analysis revealed that the electrical failures were due to shorting of stationary comb fingers to the ground plane. The first vibration related failure was an adhesion failure. The direction of vibration was suspected to cause the rubbing of two moving parts together causing adhesion. The second vibration related failure was the disconnection of linkage arms from a gear, thereby breaking a pin joint.

According to Dean et al. (2007), MEMS gyroscopes are also susceptible to high power, high frequency content acoustic noise. Acoustic energy frequency components that are close to the resonating frequency of the proof mass in the MEMS gyroscope can produce undesirable motion of the proof mass. This will likely result in undesired errors in the angular velocity measurements. If the acoustic signals possess enough power in the vicinity of the sensor resonating frequency, the resulting degradation in sensor performance can be severe enough to render the angular rate measurements useless. [86]

Example environments where this type of high power acoustic signal may be encountered include supersonic aerospace vehicles, machines that utilize high pressure nozzles, underwater applications and some audio systems [86]. The intensity level of acoustic signals is often measured in dB where 0dB corresponds to the minimum hearing threshold of a healthy human ear while 150dB corresponds to the threshold of pain in a healthy human ear.

During testing of MEMS gyroscopes under high power acoustic signals, the sound level ranged from approximately 114dB at 1KHz to 90dB at 20KHz [86]. **Most relevant findings in this investigation [86] demonstrated that** high power, high frequency content acoustic noise environments can cause degraded or even failed operation of MEMS gyroscopes. At noise levels of up to 100dB, the noise floor of the sensors' outputs were observed to increase as a function of both applied angular velocity and acoustic noise power. The acoustic excitation (near 130dB) can disrupt the sensor so that no useful data can be received reliably. Therefore, caution should be advised when using MEMS gyroscopes under environments of susceptible high power acoustic signals.

Bazu et al. (2007), tested MEMS accelerometers in a vibration environment at temperatures of $85°C$ and $145°C$ [87]. Frequency of vibration was 1500Hz and amplitude was 6G in both cases. Test duration was 200h in both tests. No visible degradation in the performance of the accelerometers during the test at $85°C$ was obtained. Testing for second sample batch was executed at a very high ambient temperature, beyond the specification limits, at $145°C$. **In conclusion:** there was very small performance degradation after 100 hours of testing. The possible failure mechanism in this case was the fatigue of the moving part of the accelerometer. [87]

Overall findings in this literature survey of vibration tests for MEMS devices can be summarised as follows:

- MEMS devices have been tested in vibration environments with accel-

erations ranging from 6G up to 120G. One test was done under high power acoustic signals where the sound level was as high as 130dB.

- There are multiple vibration parameters to vary. Most important of them being acceleration of vibration (G-value) and the spanned frequencies (Hz).
- Vibration is a very harsh environment for MEMS gyroscopes because their operation principle is usually based on coupling of primary and secondary vibration modes.
- Most likely failure types in vibration environment are adhesion, movement of MEMS joints or pins in the direction of vibration, and accelerated fatigue of the moving parts.
- There are no standard vibration tests available for MEMS gyroscopes. In one test MEMS gyroscopes were robust enough to survive a vibration of 9G's with a frequency range of 15 to 55Hz.

4.3 Environmental Testing

MEMS devices are often designed to withstand harsh environments with high or low temperature, humidity, electro-magnetic forces and corrosion. Material concerns arising from the diverse environments include stress, creep, fatigue, wave-propagation and thermal coefficient of expansion. Electrical problems apply mostly to temperature sensitivity and packaging issues dealing with shorted or broken leads. All perspectives must be addressed. [84]

Temperature tests can be of various form, i.e.:

- Constant temperature tests.
- Temperature shock tests.
- Thermal cycling tests.
- Humidity and condensation tests.

The effects of the temperature environment on the performance is of great concern since they can be a imperious source of error in micro-machined devices. **Shcheglov et al. (2000),** subjected packaged MEMS gyroscopes to various temperature environments ranging from -60 to $+60°C$. Resonant frequencies, signal drifts and quadrature drifts of the MEMS gyroscopes were monitored. **The results in this research** pointed out that temperature fluctuations are a major source of low frequency noise. The temperature affects the gyroscope through changes in gyroscope resonant frequency and drive-mode amplitude. It was also pointed out that frequency depends linearly on temperature. [88]

In an environmental test by McCluscKey et al. (2010), MEMS gyroscope signal and noise variation was measured in a stationary and a rotary test under room temperature, and then subjected to thermal cycling from -25 to $+125°C$ for 100 hours (100 cycles). The process was repeated five times for a total of 500 hours of thermal cycling. The same stationary and rotary tests were conducted after every 100 hours of thermal cycling exposure. **As a result** a permanent change in the signal was measured; the maximum angular velocity shift was $1.8°/s$ after 500 hours of thermal cycling. [89]

It is often of interest not only to measure the behavior of the MEMS electrically, but also to monitor its movement optically. **DeWolf (2004)** monitored radio frequency (RF) MEMS capacitive switches in a recent study. Monitoring was done using humidity ovens used for IC packaging. Test chamber, which is normally used under a microscope to study, for example, IR spectra or Raman spectra of different substances under varying humidity, was used for characterization of RF-MEMS capacitive switches. The humidity was changed from about 3 to 95% relative humidity (RH) within a temperature range of -10 to $+150°C$. Simultaneous optical and electrical monitoring of the devices allowed to study the effect of capillary forces on stiction of the MEMS. Stiction is defined as the friction that tends to prevent relative motion between two movable parts at their null position. [73]

It can be concluded from [73] that high humidity levels can result in capillary stiction of the moving parts of the device. Humidity can also have an indirect effect of the MEMS reliability by changing the sensitivity of insulator material used in capacitive RF-MEMS. This again might cause stiction of the moving part due to charging of the insulator.

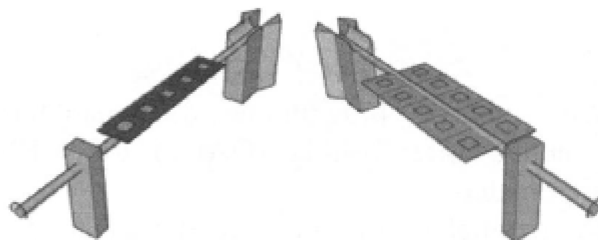

Figure 18: *Tilting variants: the axial type (left) and the wing type (right). Original image from [87].*

Bazu et al. (2007), tested the performance of MEMS accelerometers at elevated temperatures by tilting them in a thermal chamber with special equipment. Two variants (Fig. 18) of tilting movement were used for testing: the axial type and the wing type. In the axial type the accelerometers were positioned on the axis of the equipment, simulating a device placed in a car or a train. In the wing type the accelerometers were positioned at a certain distance from the axis, simulating a device placed on the wing of an airplane. Tilting tests were done at temperatures of $25°C$, $100°C$ and $125°C$. Duration of the tests were 1000h for each test. **As a result** there was no

visible degradation in the performance of the accelerometers during the tests. [87]

Overall findings in this literature survey of environmental testing of MEMS devices can be summarized as follows:

- Environmental testing parameters to be varied are usually: temperature levels, thermal cycle times, relative humidity and mixture of gases in a environmental test chamber.
- Temperature fluctuations are often the source of low frequency noise.
- Effect of temperature is also seen as a drift in angular velocity.
- Stiction, problem especially under high humidity levels, is best observed with simultaneous optical and electrical monitoring.
- Testing of MEMS accelerometers and gyroscopes can be done at elevated temperatures with a tilting or rotating device to get acceleration or angular velocity data in situ.

4.4 Gyroscope Performance Parameters

Gyroscope performance can be evaluated for example by comparing calibrated values both before and after a possible harsh loading or environmental condition (shock, vibration, humidity etc.). Relative changes in sensitivity and zero output velocity are a good indication of failure (Fig. 19). Sensitivity (Fig. 19a) (also known as scale factor) is the constant of proportionality between the actual gyroscope rotation rate about its sensitive axis and the gyroscopes output voltage. This constant is usually expressed in volts per unit angular velocity (V/dps). [8]

Sensitivity change can also be monitored as the function of temperature. Sensitivity change vs. temperature (%/°C) describes how the sensitivity will change in percentage per °C. This is a good indicator of how sensitivity is affected by temperature and helps in designing more reliable gyroscopes for different temperature conditions. [90]

Zero output velocity (Fig. 19b) (also known as bias or offset signal or the zero-rate offset) is the average over a specified time of gyroscope output measured at specified operating conditions that has no correlation with input rotation. Zero output velocity (ZRO) is typically expressed in $°/sec$ or $°/hr$. An optimal gyroscope would have a high sensitivity and minimal zero output velocity. As with sensitivity, the zero output velocity can also be monitored as the function of temperature to see how it will change per °C. [8, 90]

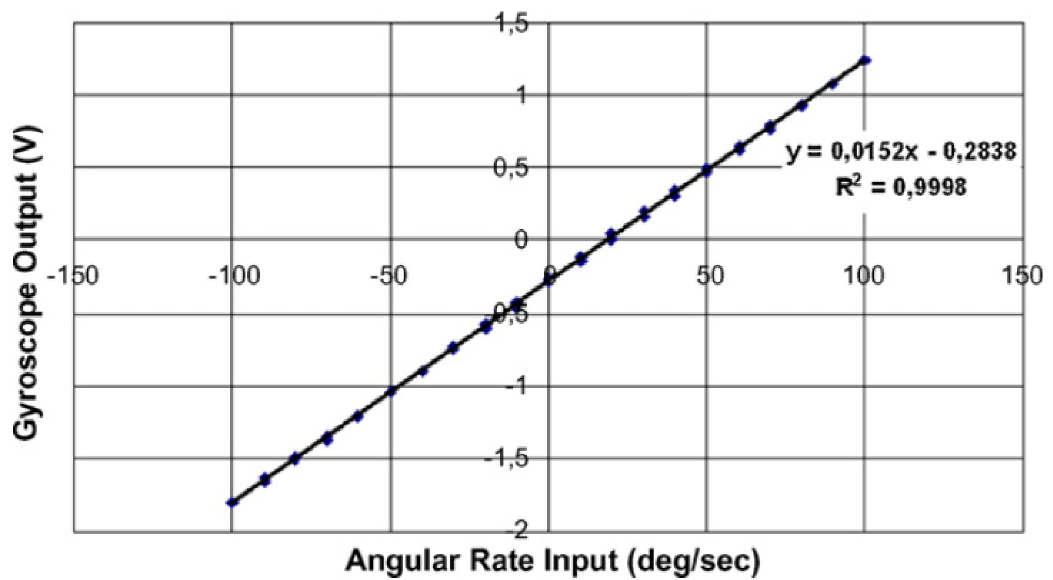

(a) *Sensitivity also known as scale factor*

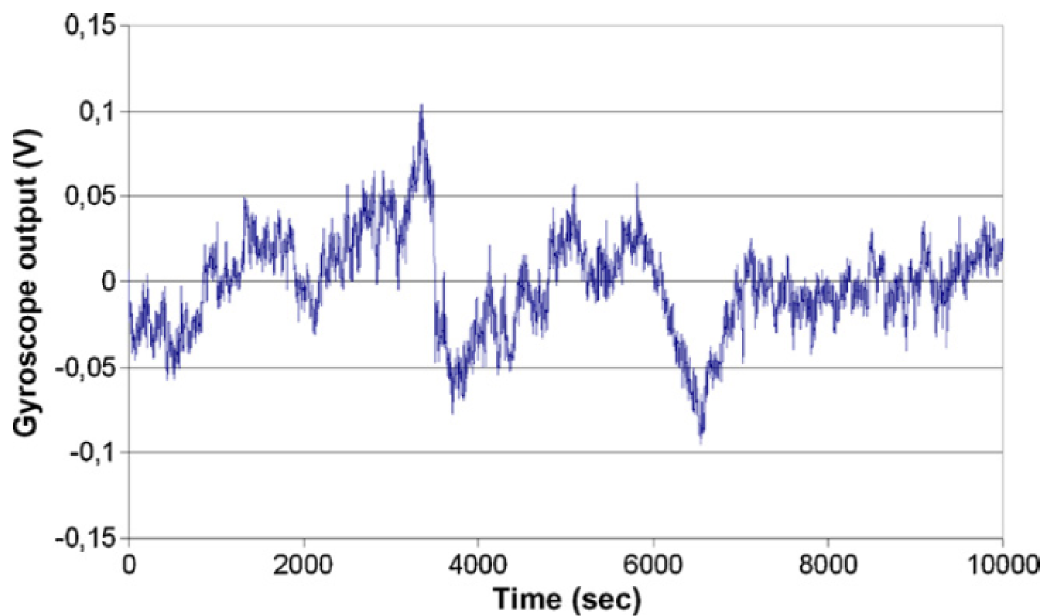

(b) *Zero output velocity (ZRO) also known as bias or zero-rate offset*

Figure 19: *Typical sensitivity plot and ZRO drift plot. Original images from [91].*

5 Research Question

This work is a part of a project that concentrates on the evaluation and characterization of MEMS devices. The project is divided into two working packages (WP1 and WP2). WP1 concentrates on the reliability assessment and evaluation of a MEMS gyroscopes. WP2 concentrates on the reliability assessment and evaluation of MEMS microphones. The project is a collaboration of Aalto University, Nokia, Okmetic, VTI Technologies and VTT, and financed jointly by these partners and the Finnish Funding Agency for Technology and Innovation (TEKES).

This work describes a part of a reliability assessment process of a 3-axial MEMS gyroscope. The objective of this thesis is to develop automated, efficient, and economical methods for the assessment of board-level reliability of MEMS gyroscopes. The focus is to develop methods to monitor the operation of MEMS gyroscopes during high-G shock impacts, vibration loadings and environmental loadings.

The board-level testing of micro-mechanical motion sensors requires the use of automated testing procedures due to the high accuracy and low noise requirements of the gyroscope components. Therefore, the selection and development of optimal test equipment and test software is critical in order to meet these requirements.

The working principles and different implementations of MEMS gyroscopes were presented in the first part of this thesis. Also presented in the first part of this thesis was the literature survey on the reliability assessment of MEMS gyroscopes in harsh environments. The second part of this thesis is the experimental part that focuses on the development of test equipment and methods for the mechanical and thermomechanical characterization of MEMS gyroscopes. The mechanical characterization consists of high-G shock impacts and vibration loadings and the thermomechanical characterization consists of environmental characterization. High-G shock impact, vibration and environmental characterization were all carried out with unique test setups.

6 Materials

This section details the 3-axial MEMS gyroscope that is the device under test (DUT). The DUT is to be characterized in environmental, high-G shock impact and vibration tests. The DUT's structure is presented, as well as the printed wiring boards (PWBs) where the DUTs are to be attached.

6.1 The Device under Test

The basic strucure of the gyroscope is presented in this chapter. The sensing element and the integrated chip, input and output pins and the communication protocols of the gyroscope are also discussed.

6.1.1 Basic Structure of The Component

The gyroscope (Fig. 20) consists of three orthogonally positioned angular velocity sensing elements to provide angular velocity output along three axes of rotation, the X, Y, and Z axis.

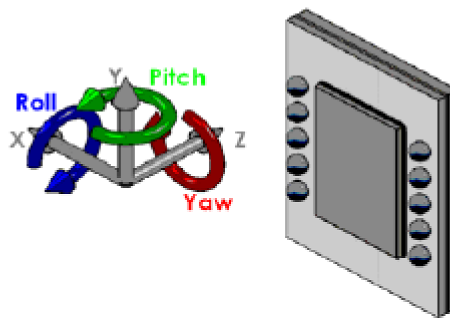

Figure 20: *The gyroscope.*

The gyroscope is designed to be very accurate (0.75 dps resolution) and low noise (noise standard deviation 0.9 dps) angular velocity measurement device. A long operational lifetime is achievable by having a low current consumption (5mA) and high stability over temperature. The device is especially targeted to battery operated devices, for example game controllers, remote controllers and mobile phones.

Communication with the gyroscope is digital. The gyro is controlled by changing the contents of the Application Specific Integrated Circuit (ASIC) registers with digital command words. The ASIC is capable of:

- Delivering synchronous digital data streams of angular velocity signals from 3 orthogonal axes.
- Performing self-test of key performance parameters.
- Making it possible to link multiple gyroscopes to provide angular velocity signals.

The angular velocity signals detected by the sensing elements are very low level and are easily lost in ambient noise. Therefore, they are amplified and transformed into digital form by the ASIC that is integrated in the package.

The 3-axial gyroscope housing is a wafer-level packaged Chip Scale Package (WL-CSP) with ten SAC405 solder bumps. The package dimensions are 3.1 mm x 4.2 mm x 0.8 mm and the weight of the package is 18 mg. Similar to the sensor elements, the package is hermetically sealed in order to prevent a variation in humidity and pressure.

6.1.2 Sensing Element

The sensing element is manufactured using bulk process. Bulk process enables to make capacitive sensors and comb-structures robust and stable. Capacitive sensors are also designed to have a low noise level and low power consumption.

The sensing element consists of one primary resonator and three secondary resonators. The ASIC drives the primary resonator while Coriolis force will couple to the secondary resonators allowing the measurement of angular velocity. Detected signal will be converted first into a phase difference and then to a voltage difference in the signal conditioning ASIC.

6.1.3 Interface Integrated Circuit

The interface integrated circuit of the gyroscope has an internal oscillator for sending clock pulses synchronizing the communication with the gyroscope and the measurement system. The device has also reference and non-volatile memory for storing and sorting gyroscope parameter data in the registers. The internal oscillator and memory enable the sensor's autonomous operation within a measurement system.

The interface between the sensing element and the device is implemented via the primary and secondary driving mode circuitry, charge-sensitive-amplifiers (CSA) and phase detector. The interface is responsible for the XYZ-angular velocity detection. After calibration and filtering in the analog domain, the signal is analog-digital converted and then filtered digitally.

Angular velocity data can be read via the serial bus and in power down mode (device's volatile registers keep their contents and the current consumption

is minimized) the device is inactive. Measurement bandwidth (20 or 80Hz) can be selected by ASIC register command.

6.1.4 Input and Output Pins

The gyroscope has ten digital input/output (I/O) pins (Fig. 21). The gyroscope can be powered with three separate supply voltage lines: analog (AVDD), digital (DVDD) and I/O supply line (DVIO), depending on the preferred application. The nominal supply voltage range is 2.5-3.0 V. Analog and digital supply voltage lines have also separate grounds (AGND and DGND).

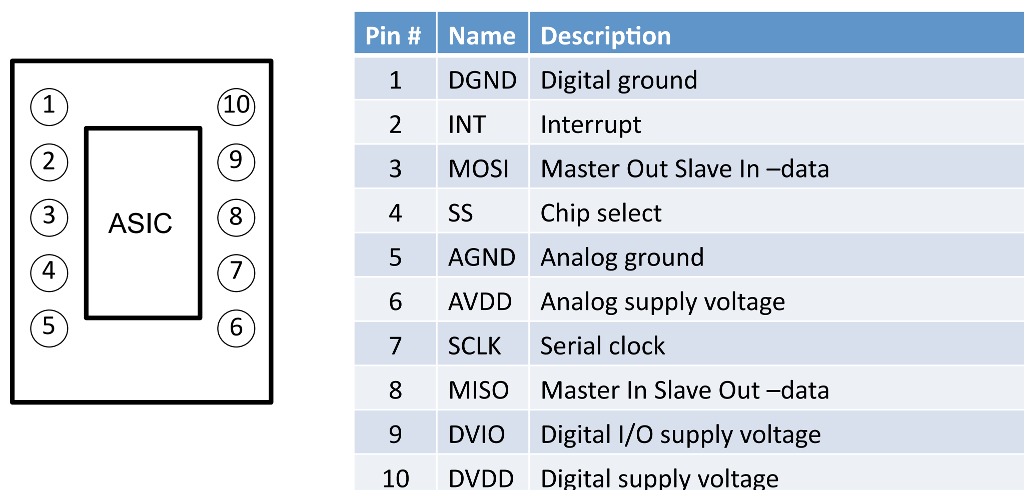

Pin #	Name	Description
1	DGND	Digital ground
2	INT	Interrupt
3	MOSI	Master Out Slave In –data
4	SS	Chip select
5	AGND	Analog ground
6	AVDD	Analog supply voltage
7	SCLK	Serial clock
8	MISO	Master In Slave Out –data
9	DVIO	Digital I/O supply voltage
10	DVDD	Digital supply voltage

Figure 21: *Gyroscope pin names and descriptions.*

The SCLK pin is used for the internal serial clock that provides pulses to synchronize the communication with the gyroscope. The interrupt pin (INT) gives an interrupt by default when each angular velocity sample is ready to be read. Interrupt conditions can be activated and deactivated via the communication bus. SS is the chip select signal pin that is used to enable gyroscope communication. The Master In Slave Out (MISO) pin and the Master Out Slave In (MOSI) pin are used mainly to send and receive data from the gyroscope. Their function is explained further in the next chapter.

6.1.5 Gyroscope Communication Protocols

Gyroscope sensor and master controller communication is based on serial data transfer and dedicated interrupt line. There are two serial interface options to choose from: the Serial Peripheral Interface (SPI) bus and the Inter-Integrated Circuit (I2C) bus. Selection of interface is done with the chip select signal pin (SS). Recommended circuit diagrams are presented in Figure 22. A 100 nF surface mounted capacitor is recommended to be placed between each supply voltage and ground level for noise filtering purposes. A

separate capacitor is recommended for the more sensitive digital I/O supply voltage (DVIO).

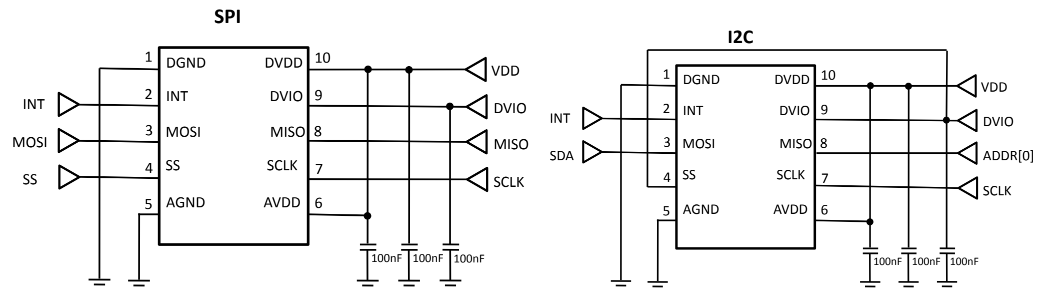

Figure 22: *Recommended circuit diagrams. SPI circuit diagram on the left and I2C circuit diagram on the right. 100 nF capacitors recommended to be placed between each supply voltage and ground level.*

The gyroscope acts as a slave on both the SPI and I2C bus. SPI bus is specified as a full duplex synchronous serial interface with 4-wires. SPI bus consists of one master device and one or more slave devices. The master is defined as a micro controller that utilizes the SPI clock signal. The slave is defined as any IC receiving the SPI clock signal from the master. In master-slave operation mode the gyroscope sensor always operates as a slave device by default. The typical SPI connection is presented in Figure 23.

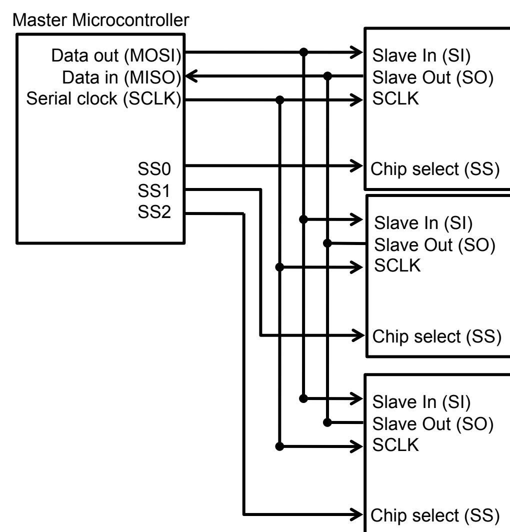

Figure 23: *SPI connection example with one master device and three slave devices.*

The SPI communication frame consists of 16 bits (Figure 24). The first 8 bits in MOSI line define information about the register address accessed and the operation mode (read or write). The first six bits are used to define the address for the selected operation that is defined by 7th bit ('0' for read

and '1' for write) followed by one zero bit. The last 8 bits in the MOSI line accommodate data for a write function and are unimportant for a read operation. Bits are sampled in from MOSI line on the rising edge of the clock signal (SCLK) and bits out from the MISO line on the falling edge of the clock signal. Data is written into the addressed register on the falling edge of the last (16th) SCLK pulse for write commands.

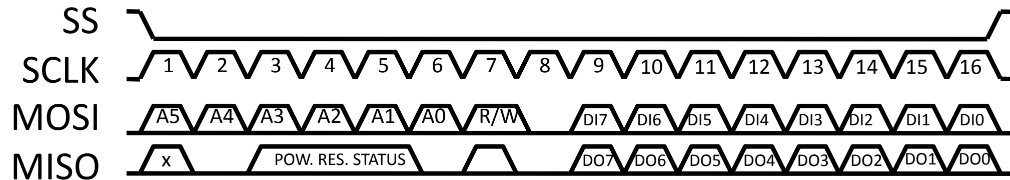

Figure 24: *SPI 16 bit communication frame format.*

The first bit in MISO line is undefined bit (bit 1, 'X'), fixed zero bit (bit 2), power reset status (bits 3-5), fixed zero bits (bit 6 and bit 8) and fixed one bit (bit 7). The last 8 data bits in MISO line are used for read operation. These data bits are zero during a write operation.

The register read command example utilizing the SPI-bus is presented in Figure 25. The master controller applies the Z-axis angular velocity register address to be read via the MOSI line: '010001' in binary format, 7th bit is set to '0' indicating read operation. The sensor replies to the request by sending the register content via MISO line with most significant bit (MSB) first and least significant bit (LSB) last. Bits DZ7 to DZ0 indicate Z-axis angular velocity data bits in the register.

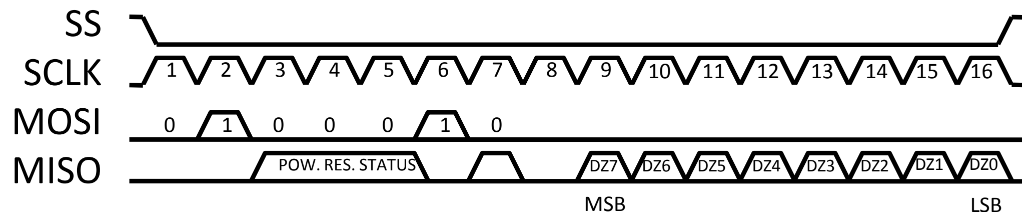

Figure 25: *Example of SPI read communication. Reading of Z-axis angular velocity data.*

SPI communication was chosen for this project over I2C, because of existing SPI bus adapter equipment and previous experience of working with SPI communication devices.

6.2 Printed Wiring Boards for Different Test Cases

Different test setups require different printed wiring boards (PWBs). The smaller board (34x30mm) is used in shock and vibration characterization. The larger board (100x100mm) is used in environmental characterization.

6.2.1 Small Board for Evaluation of the Gyroscope

To enable almost lossless kinetic energy transfer of shock impacts to the MEMS-gyroscopes, a rigid material was needed as the base material for the small board (Fig. 26). Therefore, aluminum was chosen. In addition, aluminum is good material for printed wiring boards because it is quite inexpensive and has a high strength-to-weight ratio. On the other hand, ceramic materials were also considered as a possible choice for PWB-materials. Ceramics are generally more brittle than metals, but have similar stiffness (modulus of elasticity) and similar strength, particularly in compression. Ceramics are often more expensive than standard FR4 as PWB-materials and also prone to fractures.

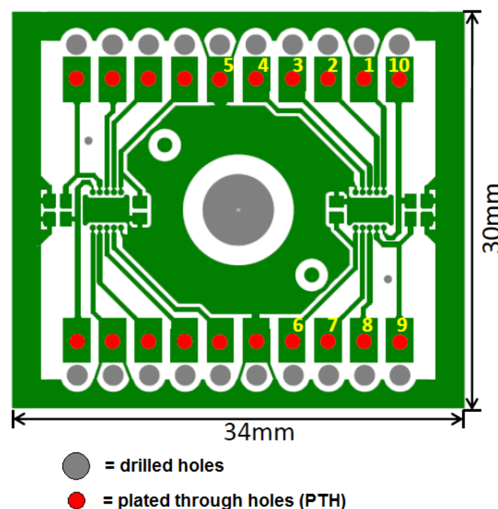

Figure 26: *Small PWB layout. Pads and their respective signals: 1. Digital ground (DGND) 2. Interrupt pin (INT) 3. Master Out Slave In -data (MOSI) 4. Chip select (SS) 5. Analog ground (AGND) 6. Analog supply voltage (AVDD) 7. Clock signal (SCLK) 8. Master In Slave Out -data (MISO) 9. Digital I/O voltage (DVIO) 10. Digital supply voltage (DVDD)*

The benefit of aluminum PWB-material is that it can absorb much of the shock impact energy without fracturing. One possible disadvantage is the fact that aluminum, as a conductive metal, might lead to some unwanted short circuits. However, these disadvantages are small compared to the risk of brittle ceramic board materials shattering catastrophically under high-G shock impacts.

Aluminum PWB-materials were favored in this work mainly because of ceramic material's possibility of brittle fracture with high-G shocks was considered a great risk. The cost of ceramic PWB-materials compared to aluminum materials was also greater. Aluminum boards are used in high-G shock impact testing and vibration testing.

6.2.2 Large Board for Evaluation of the Gyroscope

The large board (Fig. 27) is used in the environmental characterization of the DUT. The large board's material was chosen to be standard FR4 specification material. FR4 was chosen mainly because it allows the use of multi-layered structure and has a good functionality in high or low temperatures, and it is also the base material upon which the vast majority of rigid PWBs are produced.

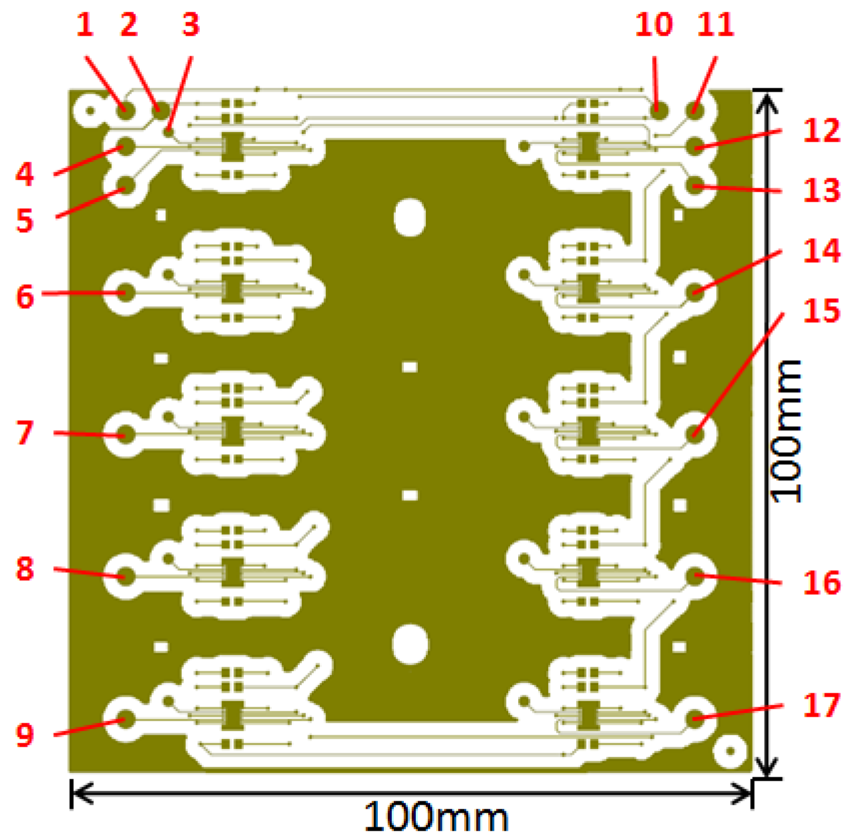

Figure 27: *Large PWB layout. Pads and their respective signals: 1. Supply voltage (V+) 2. Ground (GND) 3. Interrupt pin (INT) 4. Master Out Slave In -data (MOSI) 5. Chip select 1 (SS1) 6. Chip select 2 (SS2) 7. Chip select 3 (SS3) 8. Chip select 4 (SS4) 9. Chip select 5 (SS5) 10. Digital I/O voltage (DVIO) 11. Clock signal (SCLK) 12. Master In Slave Out -data (MISO) 13. Chip select 6 (SS6) 14. Chip select 7 (SS7) 15. Chip select 8 (SS8) 16. Chip select 9 (SS9) 17. Chip select 10 (SS10)*

FR4 employs a glass reinforced epoxy laminate sheets that are used as insulating material in PWB fabrication. The large board used in testing employs a multi-layered circuitry where FR4 epoxy layers are separating conducting copper layers. Conducting inner copper layers are connected with vias where the smallest vias (diameter up to 0.15 mm) are called micro vias. Top side of the board contains pads for soldering input and output connection wiring to.

The separate supply voltage lines (digital, analog and I/O) were connected together to form one single supply voltage line (V+). The same was done with the ground line (GND). The separate chip select signal pins (SS1 to S10) make it possible to choose which gyroscope communicates at a time. This also made possible to make only one MISO, one MOSI and one clock signal line for the board, instead of each gyroscope having an individual pin for these functions. This helped to minimize the amount of wiring needed per board and makes the large board easier to assemble and fit in the environmental characterization equipment.

7 Results of Characterization Development

This chapter describes the results of the development of the characterization equipment and methods, and the results of initial testing done with the equipment. In environmental testing, the DUT was rotated in room temperature for approximately 40 minutes, while monitoring and recording the average angular velocity for XYZ-axes, and the average temperature. In high-G impact testing the DUTs were impacted with shocks of varying G-values and visually inspected afterwards to analyze the possible damage and functionality degradation. In vibration testing, the DUT was vibrated with waveforms of various frequency sine waves and a frequency sweep. An accelerometer was used to record the acceleration of the vibrated DUT. The power spectral densities (PSDs), root mean square values (RMS) and peak values of different vibration test cases were calculated from the measured acceleration data.

7.1 Results of Environmental Characterization

The results of the environmental characterization are discussed in this chapter. The developed equipment and methods are presented before initial testing.

7.1.1 Environmental Characterization Equipment

Design criteria for the environmental characterization equipment were very challenging. The equipment would have to work reliably under the same harsh conditions that the gyroscopes are to be tested in. These harsh conditions include: high temperature (+125°C), low temperature (−40°C), humidity (over 90% RH) and multi-gas mixtures, and different combinations of these conditions. The equipment would also need to survive thermal cycles from one extreme temperature to the other and even under high humidity.

Thermal testing times are usually hours, days or even months so the preferred method for characterization was to be automated and allow characterization of multiple samples. Measurement of angular velocity along X, Y and Z -axis was designed so that there would be only one rotating axis to measure equal output in all three. This allows the rotating device (motor and axle) to be compact and require only one rotating axle instead of three.

In order to get angular velocity of equal magnitude from all three axes (X-Y-Z) of the gyroscope, while rotating the boards in only one direction (be it clockwise or counter-clockwise), each gyroscope board (PWB) is oriented at an angle of 35.26° (Fig. 28) from the rotating axis. This makes the gyroscope components axes to be at an equal angle (54.74°) from the rotation axis (Fig. 29).

For example, if the rotation device is rotating at a constant angular veloc-

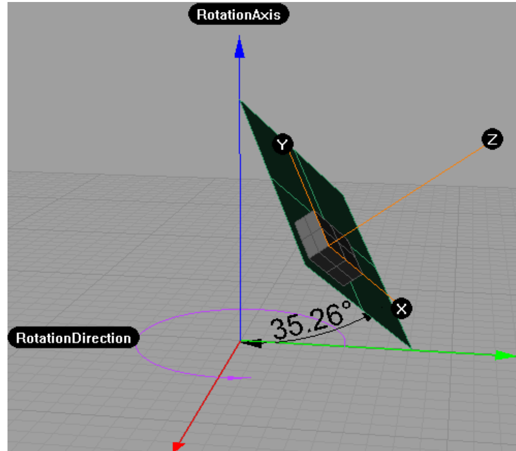

Figure 28: *Gyroscope board orientation. The 35.26° angle from the rotating axis (in blue). Rotation is counter-clockwise (in purple) around the rotating axis. The gyroscope's axes (XYZ) are marked as text annotation dots.*

ity Ω_{rot}, the magnitude of angular velocity around the Z-axis of MEMS-gyroscope can be calculated from the vector projection of the reference angular velocity with

$$\Omega_z = \Omega_{rot} \cos(54,74°) \tag{12}$$

where Ω_z is the angular velocity around the Z-axis of the gyroscope, Ω_{rot} is the angular velocity of the rotation device (the reference) and $54,74°$ is the same angle between each axis (X-Y-Z) of the gyroscope and the axle of the rotating device (Fig. 29).

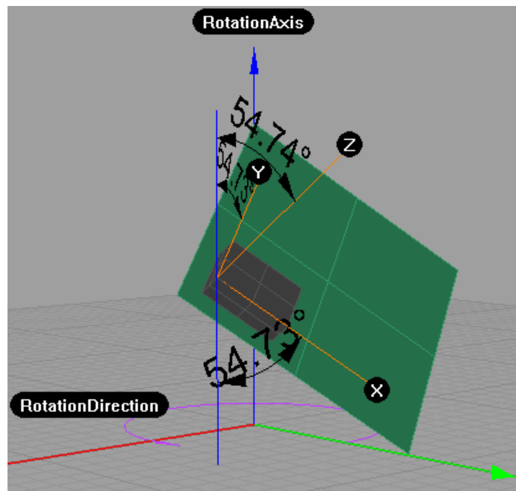

Figure 29: *Vector projection of angular velocity. Gyroscope X-Y-Z axes colored in orange and rotation device axis in blue. The small difference (0,01°) in two angles is because of rounding in the 3D-modeling tool used.*

Inserting the value $\Omega_{rot} = 1873,53\ dps$ (maximum speed of the rotation device) to the equation (12) we get $\Omega_z \approx 1081\ dps$. Using the same equation, as the angles are equal, for X- and Y-axis we get $\Omega_x \approx 1081\ dps$ and $\Omega_y \approx 1081\ dps$.

The materials for the characterization device mechanics were required to withstand high temperature fluctuations and humidity in long use. Three different options for the materials of the device mechanics were considered: aluminum, stainless steel and plastic (polyvinyl chloride, PVC). Plastic was considered as easy as metals to work with, but the need to withstand high temperature made the choice of metals more suitable. The corrosion resistance under long term humidity favored stainless steel over aluminum. Aluminum also has higher thermal coefficient of linear expansion than stainless steel ($\alpha_{Al} = 23 * 10^{-6}/°\text{C} > \alpha_{Fe} = 17.3 * 10^{-6}/°\text{C}$) [92]. Thermal expansion was considered a risk if the rotating mechanical parts would expand too much and hinder the rotation by getting stuck. This also made the choice of contacting materials with dissimilar thermal expansion coefficients unsuitable. As a result, stainless steel was chosen as the main material for the mechanical parts of the rotation device.

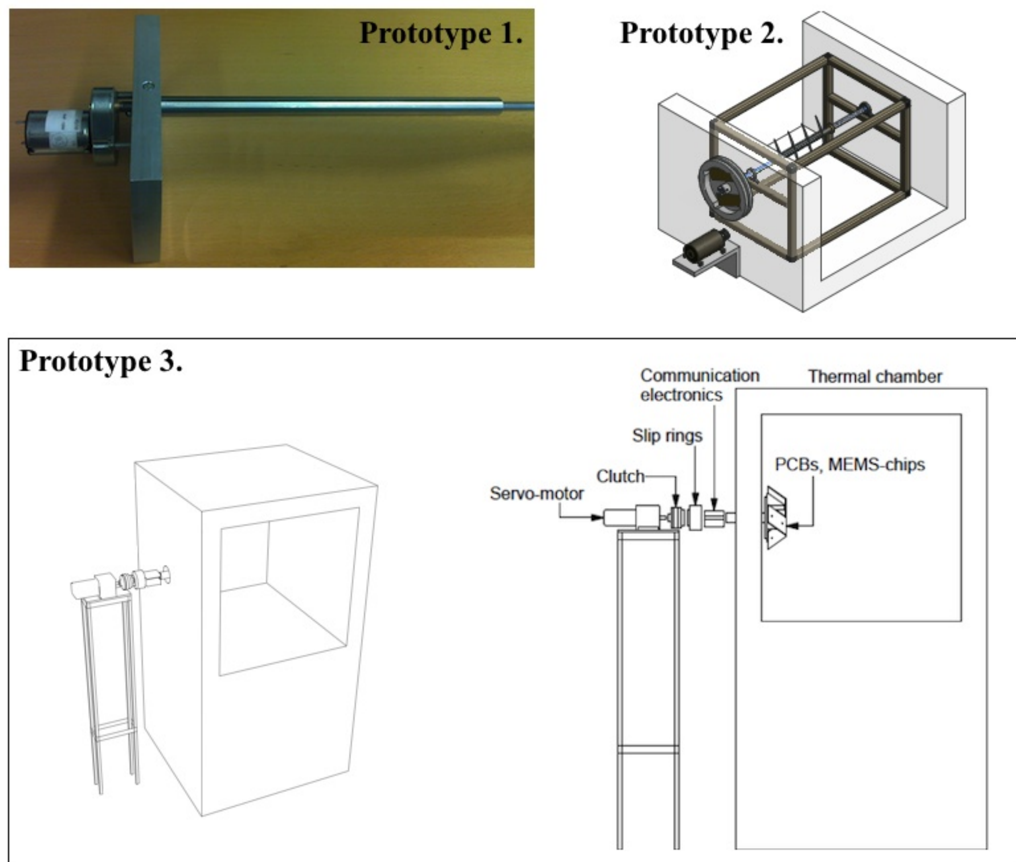

Figure 30: *Evolution of the designs for the rotation device.*

In the course of the project, the design of the rotation device for the en-

vironmental characterization evolved, as seen in Figure 30. On the upper left-hand corner of Fig. 30 is the first functioning prototype. The prototype consisted of a rotating axle connected to a direct current motor (DC-motor). The gyroscope printed wiring boards were designed to be placed through the axle like meat on a barbecue stick, hence the name "barbecue stick design". In this design, it was learned that the rotation velocity and accuracy of the DC-motor were inadequate. The motor was considered not stable enough for accurate angular velocity measurement purposes. The first prototype also raised the question of how to power the gyroscopes under rotation.

In the second prototype (upper right-hand corner of Fig. 30) the placement of the gyroscope printed wiring boards was worked through in more detail. The gyroscopes were suggested to be placed in the middle of the axle to even the heat distribution, as the heat distribution tends to concentrate in the center region of the thermal chamber. One of the issues in the evolved barbecue stick design was the problem of attaching the boards to the axle at the precise angle of 35.26°. This would have required drilling an skewed oval hole to the center of the printed wiring boards and place precisely machined spacers (like nuts or metal washers) between each board. Taking the middle or last gyroscope board out for inspection would then have required to take out the spacers and boards before it, one by one, making the installation time consuming, because of having to detach wiring between each board.

A flywheel was considered for this design to add stability to the rotation by balancing the mass of the axle. This design was quite robust and contained a frame with bearing housing on both ends to support the rotating axle. One of the issues in placing such a robust frame inside a thermal chamber is the added mass. The more the mass there is inside the chamber the longer time it takes the mass to heat and cool. This would have probably added unnecessary time delays to the thermal cycling of the gyroscopes, as they are the device under testing. One of the important design points was to make the device compact and minimize the amount of heating mass inside the thermal chamber. The ease of detaching the gyroscope boards out for inspection, and attaching them back again, was also an important design point. These points lead to the third protype seen in the lower left- and right-hand portion of the Figure 30.

The finalized rotation device (Fig. 32) consists of a servo-motor, jaw coupling (clutch), electric slip rings, communication electronics and a rotating jig to fit three large FR4 boards. The rotating jig is made out of stainless steel and it is to be placed inside a thermal chamber. The current system is capable of recording output data from up to 24 gyroscopes, one at a time. It is also possible to add multiplexer to the setup to increase the amount of measurable gyroscopes. The mechanichal parts of the rotating device are presented in Figure 31.

The servo-drive that controls the servo-motor is controlled with a PC. The servo-drive has also an option for a remote control or input-output-interface (I/O) controlling with an analogue jog wheel or digital switches. The servo-

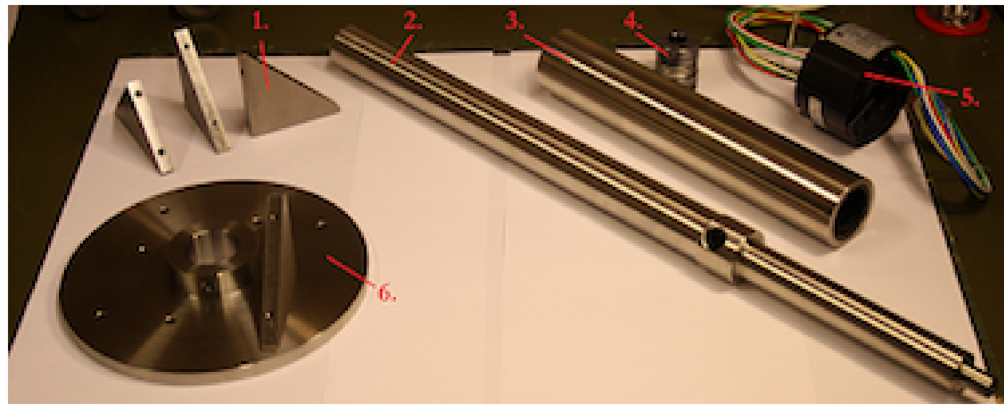

Figure 31: *Mechanical parts of the rotating device on a table before assembly. Starting from top-left: 1. Supporting block for PWB. 2. Rotating axle. 3. Outer part of the rotating axle. 4. Coupling. 5. Electric slip rings. 6. Support jig made from stainless steel.*

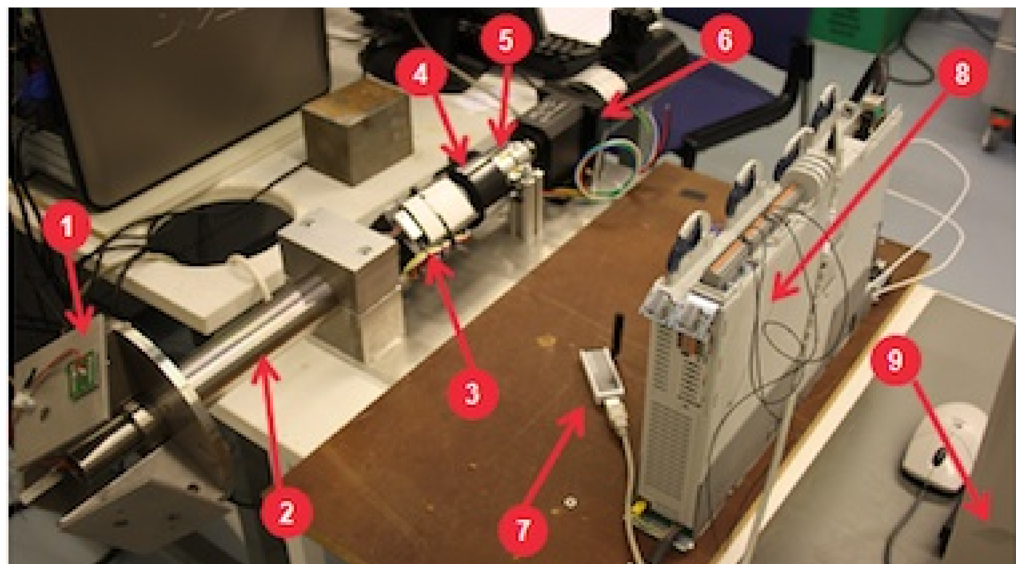

Figure 32: *The rotation device: 1. Rotating jig, gyroscope PWB 2. Outer shell, rotating axle inside 3. SPI-bus and USB-hub 4. Slip rings 5. Coupling 6. Servo-motor 7. Wireless USB transmitter/receiver 8. Servo-drive 9. PC, with control and measurement software.*

motor is programmable with different speed ramps, where acceleration and deceleration times can be adjusted. The rotating axle is connected to the motor with a regular jaw coupling (clutch). Servo-motors were considered suitable for this project because they are quite economical (obtainable for under €1400) and provide good stability and accuracy as they are intended to be used in high-precision applications such as robots and positioning in conveyer belts.

Communication link to the gyroscopes is provided with a wireless USB hub, wireless USB adapter and a SPI bus adapter (Fig. 33). The gyroscopes' signals are connected directly to the SPI bus adapter. The SPI bus adapter

is connected to the USB hub that sends angular velocity data wirelessly to the receiving USB adapter. The receiving USB adapter is connected to a PC. The angular velocity data can then be analyzed at a later time. The wireless communication was tested successfully with an early prototype of the rotating device. In the early prototype the powering of the wireless USB hub was done with a regular 9V battery while the device was in rotation. There were no significant communication or power issues, but batteries were not suitable for the final design because of the need to replace or reload them from time to time.

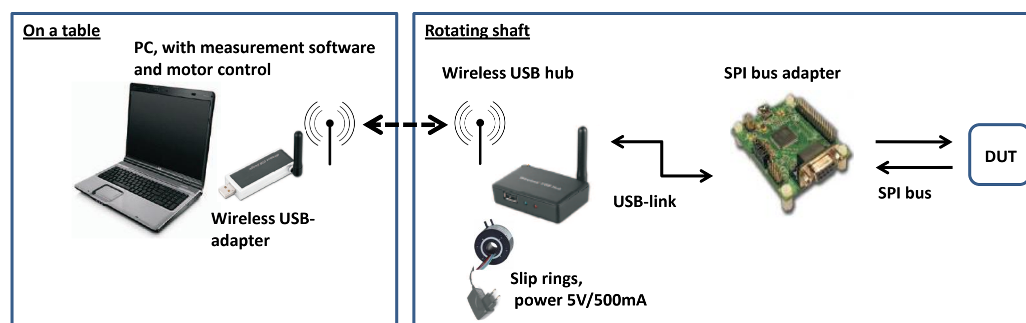

Figure 33: *Illustration of the communication electronics.*

The powering of the necessary communication electronics and the gyroscopes in the final design is implemented via slip rings (also called rotary electrical interfaces, rotating electrical connectors, swivels or electrical rotary joints). The slip ring is a mechanism of making an electrical connection in a rotating assembly. The very same technology is used in steering wheels or wind turbines. The slip rings allow the powering of the system even in very high speeds (up to 1000 rpm, according to the manufacturer's specification).

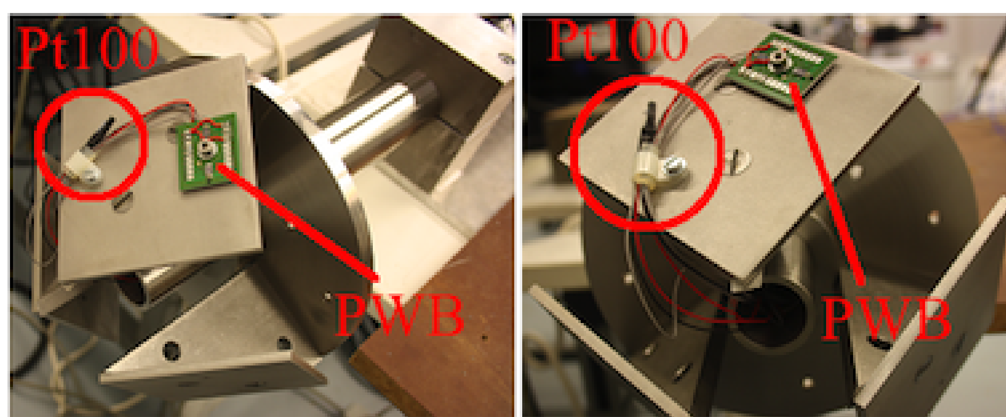

Figure 34: *Pt100 temperature sensor placement and one small gyroscope PWB. Wiring is put through the rotating axle as seen on the right.*

The temperature of the gyroscopes is measured with an external sensor placed as close as possible to the rotating gyroscopes (Fig. 34). The thermal and

humidity chamber has some means of outputting temperature data, but implementing it in an automated test setup was considered too laborious and complicated. The external sensor is a standard platinum resistance thermometer (Pt100). Pt100 operates on the principle of predictable change in electrical resistance of platinum with changing temperature.

7.1.2 Methods for Environmental Characterization

To fully characterize MEMS gyroscopes, one must also examine the effect of environment on their critical performance parameters. In this case, the gyroscopes are to be rotated at constant angular velocity in temperature and humidity chambers. The suspected main effect of temperature is the drift of angular velocity, and the suspected main effect of humidity is stiction, based on the literature survey presented in Chapter 4.

In addition to the temperature or humidity level, the rotation speed and rotation time in the chamber could also be varied. For example the rotation time can be set freely or defined by how much time before the next temperature step is reached (Fig. 35). When the temperature has set to a wanted level (i.e. room temperature or maximum) the servo-motor starts to rotate the gyroscope boards at predetermined angular velocity.

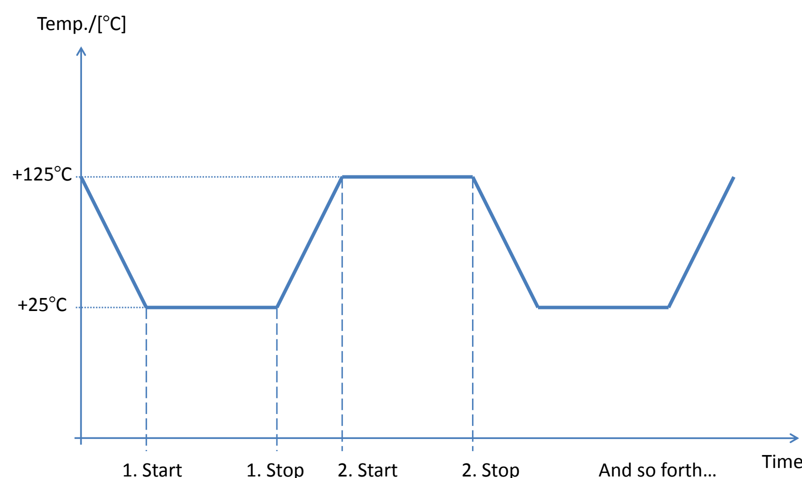

Figure 35: *Example of a thermal cycle altering between +25°C and +125°C. Cycle starting and stopping points on x-axis (time).*

The measured angular velocity output of the gyroscopes can be compared to a reference angular velocity. The reference angular velocity is given by the rotating servo-motor's integrated tachometer. The angular velocities in the X-, Y- and Z-direction of the gyroscopes can be plotted as a function of

temperature, in order to characterize the effect of the temperature drift on the gyroscopes.

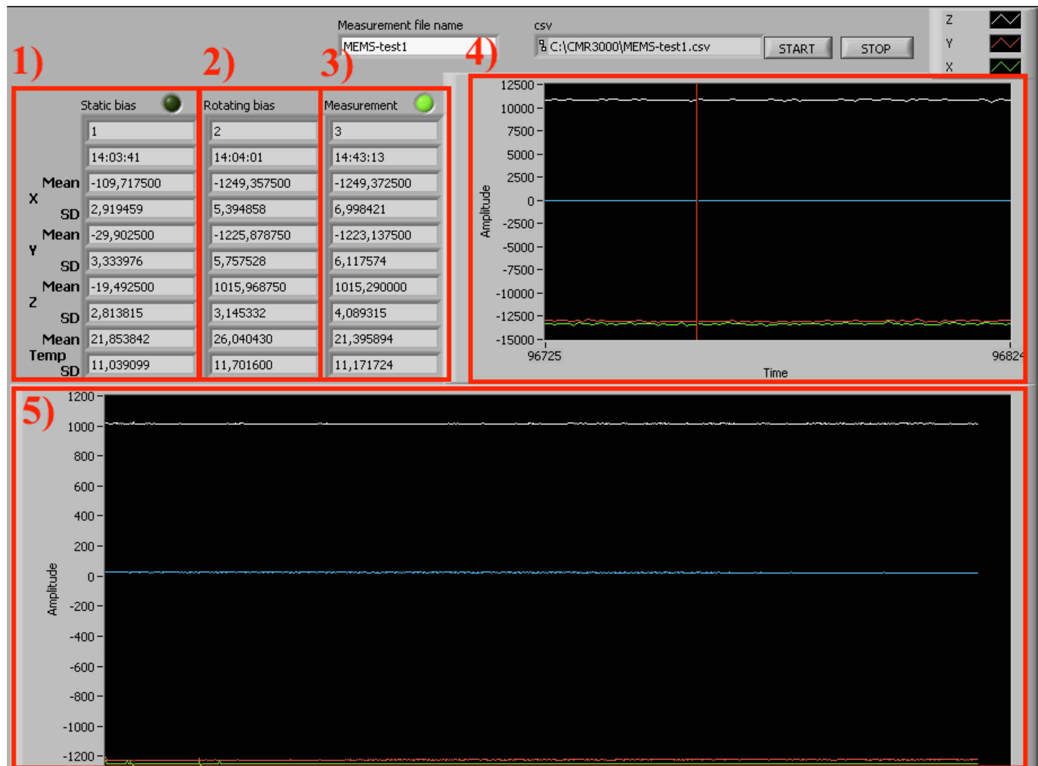

Figure 36: *Screenshot of the measurement software, courtesy of Mr. Matti Linnavuo. (1) Static measurement column (2) Reference measurement column (3) Continious measurement column (4) Monitor for 100 measurement points (5) Monitor for the whole measurement.*

A screenshot of the measurement software for reading and recording angular velocity data is presented in Figure 36. The sofware is capable of recording mean angular velocities from X, Y and Z -axis of the gyroscope. The standard deviation (SD) of angular velocities is also calculated and presented in the software. The mean temperature, using an external sensor, and standard deviation of temperature is also recorded and displayed on screen. Software was developed with the National Instruments Labview application that is specially designed for test, measurement and embedded systems.

The first column in the measurement software is the static measurement column (1), it is displayed once as the zero speed (0 rpm) of the rotating device is measured. After static measurement is recorded, the program prompts the user to start the rotating device. The starting is done automatically in the final version of the test software. The second column is the reference measurement column (2) that displays the first measurement when the motor has started and accelerated to its full speed (i.e. 1870 dps). Then the measurement keeps running until it is stopped by user and angular velocity values are displayed in the continious measurement column (3).

The measurement software has two monitors: monitor for 100 measurement points (4) and monitor for the whole measurement (5). Monitor for 100 measurement points displays the angular velocities of X,Y and Z -axis for hundred measurement points. Taking hundred measurements takes approximately 4 ms of time. The mean and standard deviation of angular velocity and temperature is calculated from these hundred measurement points. Monitor for the whole measurement displays these mean angular velocities for the whole measurement time (e.g. for 40 minutes). In other words, the 100 measurement points displayed in the upper right-hand corner monitor (4) present one pixel in the whole measurement monitor (5).

Angular velocity data and temperature data is stored in an Excel-file that can be used for later analysis and archiving purposes. Each row in the Excel-file holds mean angular velocity and standard deviation data, as well as temperature data, for 100 measurement points. Therefore, 40 minutes of measurement contains approximately 800 rows of data.

7.1.3 Testing of Environmental Characterization Equipment

This section is about the initial measurements done with the rotation device (Fig. 32, p. 44). One small aluminum gyroscope board was connected to the rotating device. The gyroscope is aligned at a specific angle ($35,26°$). This alignment allows to measure the same angular velocity from all three axes (XYZ) while simultaneously rotating the axle in only one, clockwise or counterclockwise, direction. Temperature sensor was placed near the gyroscope board to measure possible temperature changes during the test. The gyroscope was attached to the communication electronics with wiring through the rotating axle.

The gyroscope was rotated in the negative direction (counter-clockwise) for approximately 40 minutes in room temperature ($\sim 25°C$) at a speed of 312,25 rpm that equals 1873,53 dps. The chosen speed is the maximum speed of the rotating device's servo-motor and is very near the actual measuring range of the gyroscope, which is 2000 dps. The results of the 40 min test run are presented in Table 1. Figures of the measured angular velocities for the X, Y and Z -axis as a function of time are presented in Figure 37.

Table 1: *Results for the 40 min test run with reference angular velocity of 1081 dps in the negative direction.*

	Arithmetic mean	Average standard deviation
X-axis	-1249,81 dps	7,13 dps
Y-axis	-1222,94 dps	6,38 dps
Z-axis	-1015,07 dps	4,17 dps
Temperature	23,18°C	11,25°C

The reference values of angular velocity are calculated (from Eq. 12, on p. 41)

to be approximately 1081 dps for each axis. Table 1 shows that the measured X- and Y-axis average angular velocities have an offset of 142 and 168 dps (1081 dps - 1249,81 dps = 142 dps). The average angular velocity of Z-axis is more stable with only 66 dps offset. The uncalibrated temperature shows a fairly large standard deviation of 11,25°C and it can be considered too large for accurate measurements. Nonetheless, the measured total average temperature seems reasonable (23,18°C).

Linear dashed trend-lines were added to the angular velocity figures, in order to see better if the average angular velocity is increasing or decreasing as the function of time. The X-axis average angular velocity (Fig. 37a) and the Y-axis average angular velocity (Fig. 37b) appear to be drifting towards more positive values. This may be an indication of small temperature drift. However, Z-axis average angular velocity (Fig. 37c) is very stable with only a slight deviation towards a more negative value.

Obviously, further testing and a larger sample size are required to verify any positive or negative correlation between angular velocity and temperature, but failure analyses are beyond the scope of this work. Results for the 40 min test run verified that the rotation device is capable of measuring angular velocity accurately and works as designed.

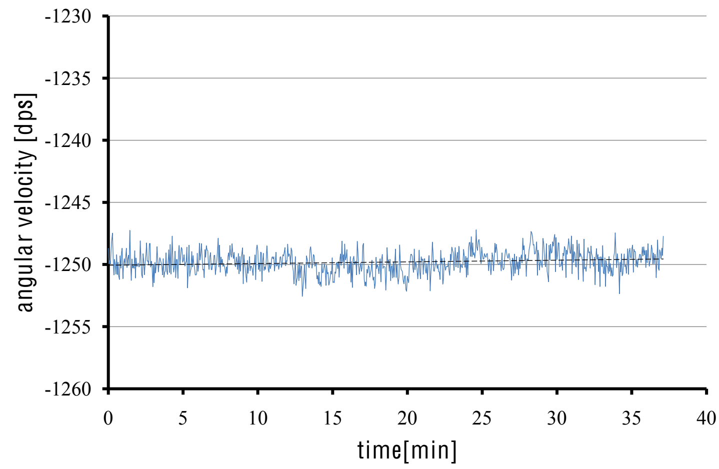

(a) *X-axis mean angular velocity.*

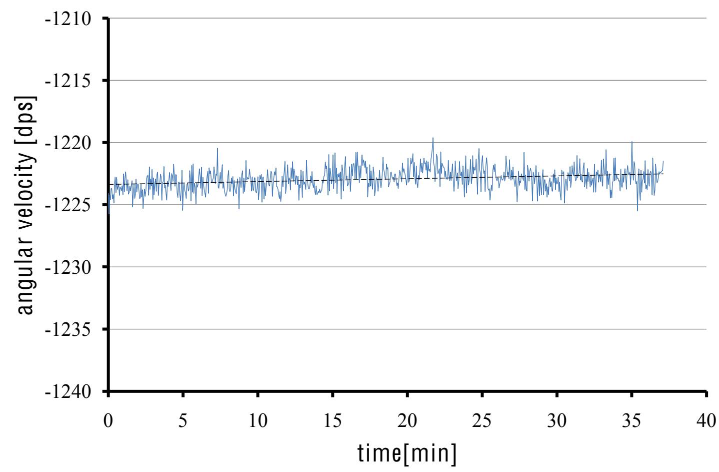

(b) *Y-axis mean angular velocity.*

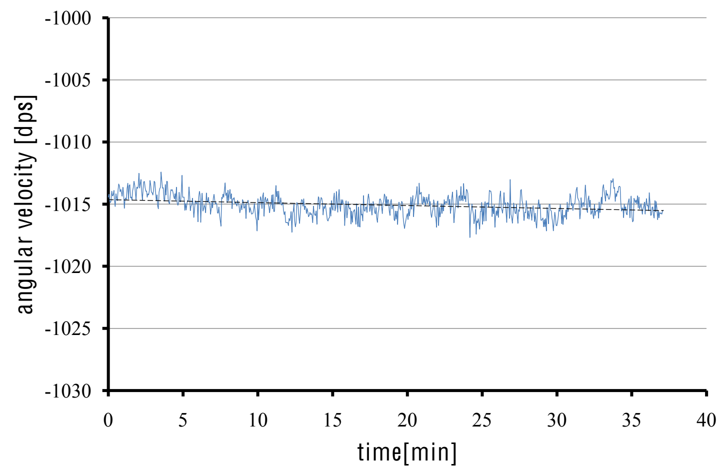

(c) *Z-axis mean angular velocity.*

Figure 37: *Mean angular velocities.*

7.2 Results of High-G Shock Impact Characterization

The results of the high-G shock impact characterization are discussed in this chapter. The developed equipment and methods are presented before initial testing.

7.2.1 Shock Characterization Equipment

Shock characterization equipment included a pneumatically assisted shock tester (Fig. 39) that relies on mechanical impact to generate the necessary high-G shock pulse. The samples were connected to a stainless steel jig (Fig. 40) that should not bend or deform too much under high-G shock impacts. The possible deformation of the steel jig was analyzed with software capable of Finite Element Method (FEM) analysis (Fig. 38). It was concluded from this analysis that the jig is capable of surviving shocks up to 65 000G:s with only slight deformation. With 480 000G:s there was considerable deformation as seen on the left-hand side of Figure 38.

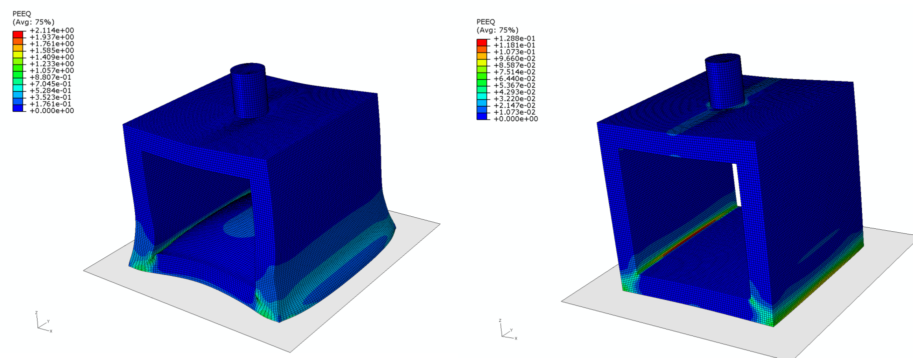

Figure 38: *FEM analysis of shock characterization steel jig deformation under 480 000g (left-hand side) and 65 000g shocks (right-hand side). Photo courtesy of Mr. Jue Li*

The FEM analysis aided the design of the jig. Based on the simulation results, the edges of the jig were rounded to lessen the shock load in them. Small channels for wiring were also machined on the surfaces of the jig. These channels are underneath the gyroscope boards as seen in Figure 40. This allows the boards to be glued on the jig and also to fit the wiring for them.

Deceleration values that can be reached with the current setup are up to 80 000g:s. Maximum impact repetition frequency is approximately 1,6Hz. Main benefit from the pneumatic shock impact tester is that it has better repeatability and stability of the impact pulse over the traditional traveling table drop test method.

The pneumatic shock impact tester consists of a pneumatic cylinder (2) with a piston (3) that has a removable shock absorber and a stainless steel jig (4)

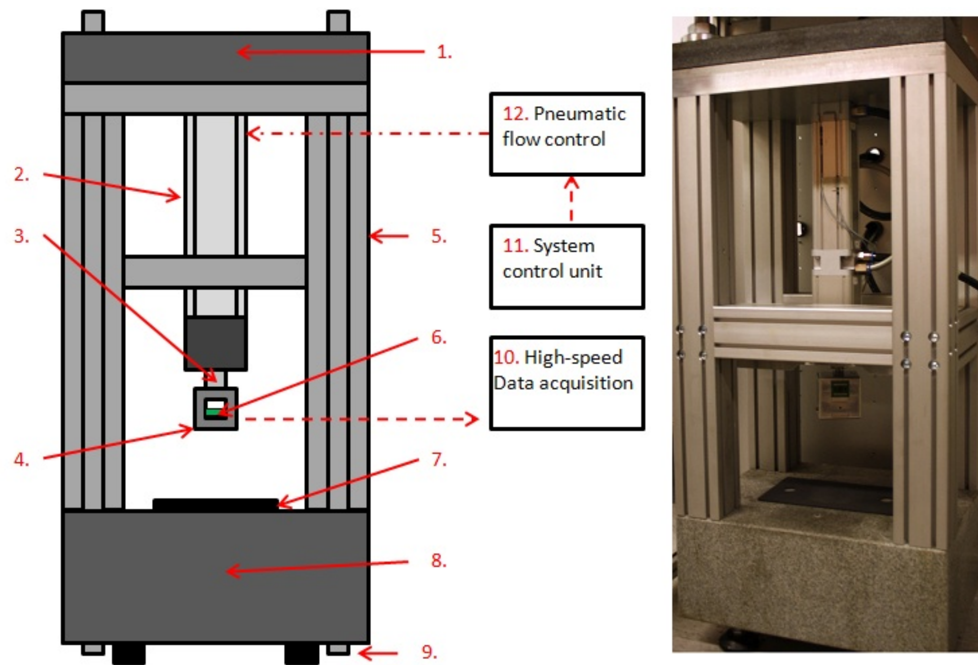

Figure 39: *Pneumatic shock impact tester. Image adapted from [93].*

to hold the samples. Shock impact tester framework is made out of aluminum (5) and it is attached on top of a rigid impact surface (8). Stabilization of the structure and reduction of excess vibration is achieved by drilling side pillars (9) through the top (1) and bottom (8) stones.

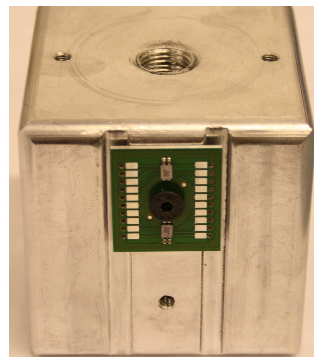

(a) *Jig from the side.*

(b) *Jig from the top.*

Figure 40: *Stainless steel jig for the attachment of the gyroscope PWBs in different orientations for the shock impact testing.*

A suitable shock pulse is achieved by covering the strike surface with different foam rubber mats (7). A lightweight accelerometer is attached on top of the sample (6) for measurement of deceleration. The pneumatic shock impact tester is operated with a control unit (11) that controls the air flow and pressure with a valve and a pressure chamber (12). A high-speed data

acquisition system (10) can be used to record the number of shocks to failure.

7.2.2 Methods for Shock Characterization

The gyroscope angular velocity should be measured before and after a impact (Figure 41) to see any changes in gyroscope performance. Unless the first impact is so powerful that the gyroscope is clearly and visibly broken. Impacts are varied by changing the G-value, amount of shocks and duration time of the shocks. The PWBs that contain the gyroscopes can also be impacted from different sides to vary the effect of impacts even more.

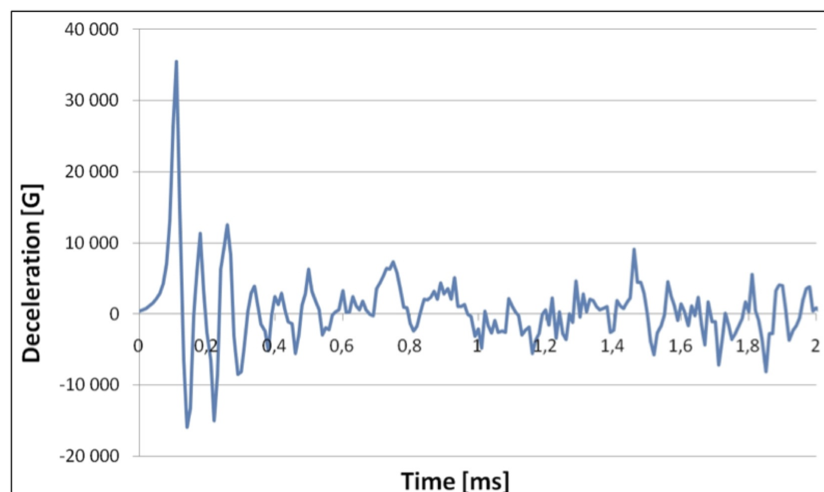

Figure 41: *Example of a shock impact pulse that has amplitude of 35500G and 0.12ms pulse width (measurement of pulse width starting around 2000G).*

To summarize, the high-G impact shocks can be varied by

- changing the G-values,
- changing the duration time of the shocks,
- changing the frequency and number of shocks,
- and adjusting the impact area and site of the shocks.

The gyroscopes output can be measured after each impact by detaching the stainless steel jig from the the setup and placing it on a rate table or a rotation device. The gyroscopes output could also be measured after a series of of impacts, but this is inadvisable, because it is then very difficult to realize at what instant (G-value, shock duration, etc.) did the fault actually occur.

7.2.3 Testing of High-G Shock Impact Equipment

Performance of the high-G shock impact test equipment, with the stainless steel jig attached, was evaluated with six measurements. Test values are

presented in Table 2. The pneumatic pressure of the high-G impact tester was gradually increased during the first five measurements. Output pressure was increased to the maximum value for the final, sixth, measurement.

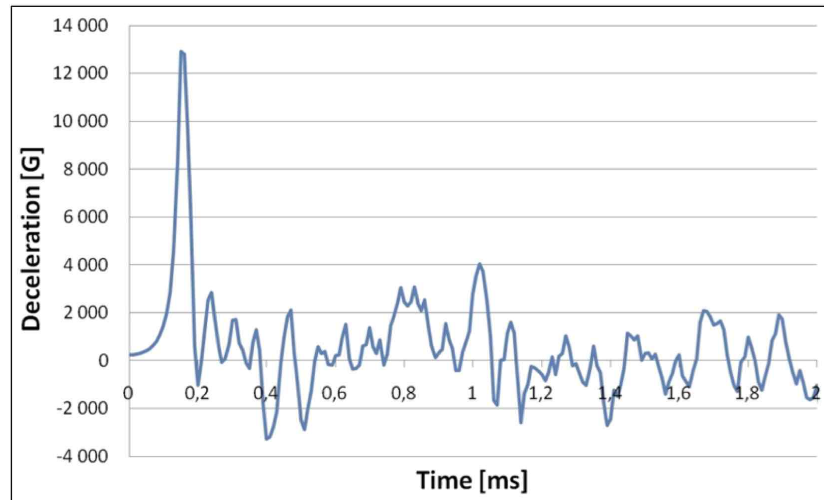

Figure 42: *First measurement, peak value 13000G and 0.2ms pulse width (measurement of pulse width starting around 2000G).*

Figure 42 shows the shock impact pulse of the first measurement. It can be remarked that the pulse width shortened from 0.2ms to 0.12ms with the increasing G-value. The pulse width can be altered with foam rubber mats, of different thickness, on top of the surface stone.

Table 2: *Shock impact values for the six measurements conducted.*

Measurement nr.	Peak value [G]	Pulse width [ms]
1	13000	0,20
2	16500	0,19
3	18000	0,18
4	20000	0,16
5	22500	0,14
6	35500	0,12

Three small aluminum-boards with dummy (ASIC in-place, but no angular velocity response) gyroscopes were attached to the jig in three different orientations (Fig. 43). The output of the test equipment was set to achieve the maximum impact value of 35500G.

All tested gyroscopes failed after the first shock impact. The failed surfaces of the gyroscopes are presented in Figure 44, and in more detail in Figure 46. Rest of the detailed images of the failed gyroscopes are presented at the end of this work in Appendix II and Appendix III.

Comparing the images of failured gyroscopes to the cross-section layout of the gyroscope (Fig. 45) it can be seen that the failed structures have fractured

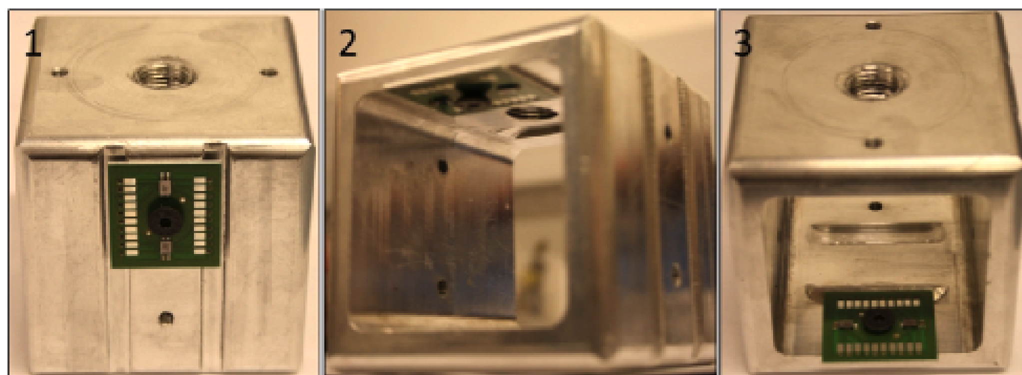

Figure 43: *Used orientations of the jig with tested gyroscopes.*

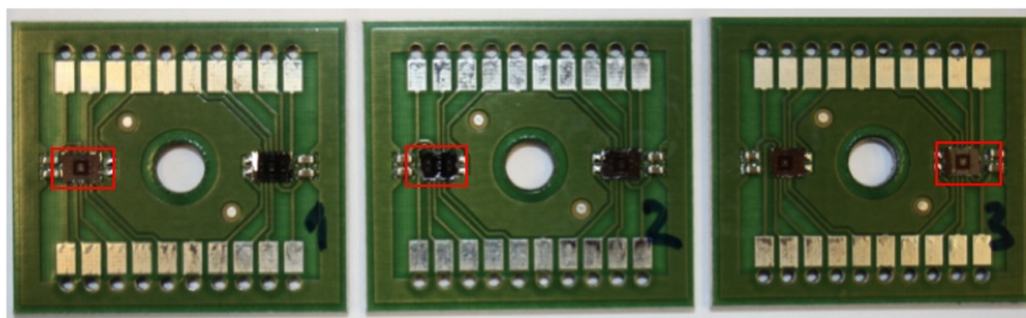

Figure 44: *The failed gyroscopes. The structures boxed in a red line have been enlarged in the following images (Figures 46-55).*

very near the glass layer at the anodic bonding interface. Further testing and failure analyses, which are beyond the scope of this work, are required to determine whether the fracture always starts at the anodic bonding interface or does it sometimes start inside the borosilicate glass layer.

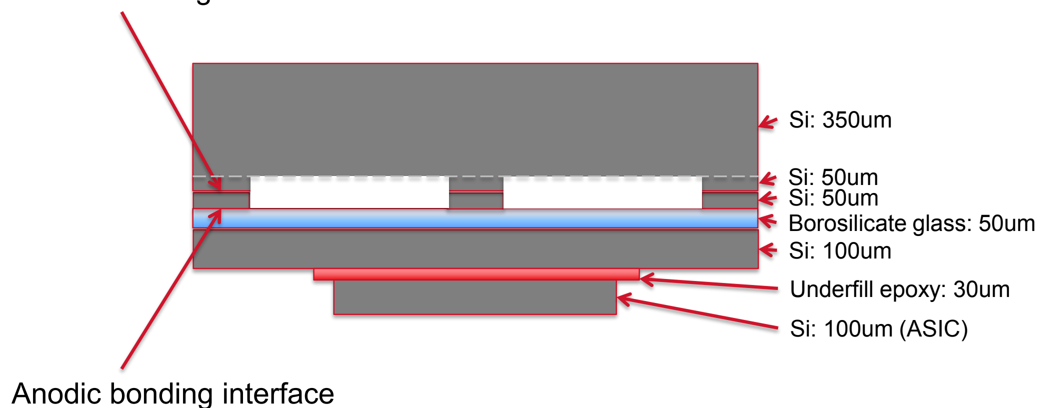

Figure 45: *Cross-section image of the gyroscope.*

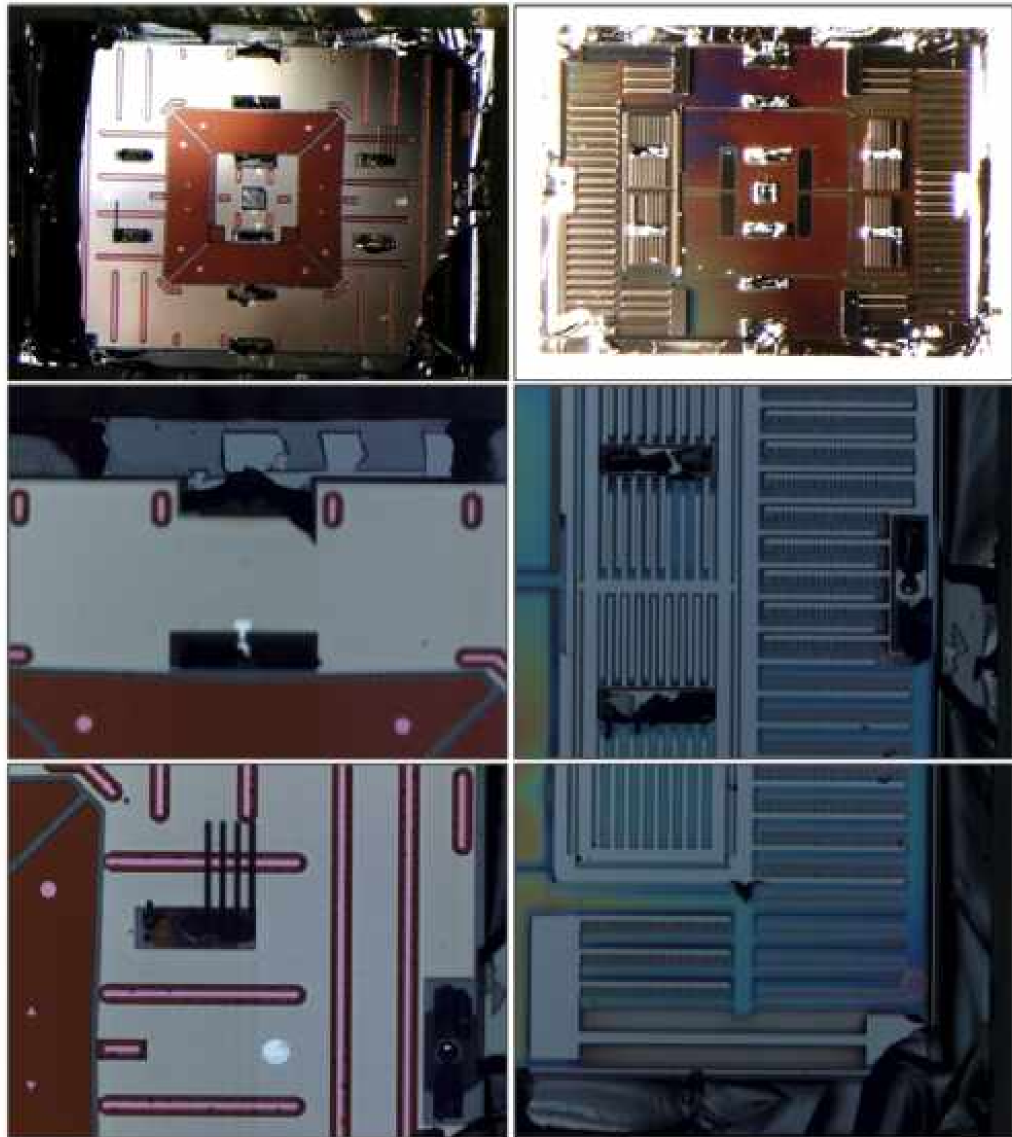

Figure 46: *The failed structure of gyroscope 1. The left-hand column is the structure that stayed attached to the board and the right-hand column the structure that broke-off.*

7.3 Results of Vibration Characterization

The results of the vibration characterization are discussed in this chapter. The developed equipment and methods are presented before initial testing.

7.3.1 Vibration Characterization Equipment

Vibration characterization equipment (Fig. 47) include a waveform generator and a vibration shaker. The waveform generator is capable of outputting different waveforms with different frequencies (e.g. 6000Hz sine-wave or random noise). The waveform generator can also perform frequency sweeps with adjustable time period (e.g. sine-wave from 20Hz to 10kHz, in 20s). The waveform generator has two output channels.

The output of the waveform generator is connected to the input of the vibration shaker, and then the vibration shaker starts to vibrate ideally with the same frequency and amplitude of the generated waveform. The vibration shaker has an adjustable gain level to increase the amplitude of the vibration. The maximum input frequency of the shaker is 13kHz. The vibration shaker is fitly suited for general purpose vibration testing of small components and sub-assemblies.

The gyroscope PWBs can be attached to the vibration shaker with a small metal rod that is screwed on top of the shaker. They can also be screwed directly on top of the shaker. The metal rod allows the gyroscopes to be tested for example inside a thermal or humidity chamber while the shaker is placed outside the chamber. The shaker itself can be mounted on a surface through screw holes underneath the shaker.

Figure 47: *The vibration characterization equipment: 1. Waveform generator 2. Vibration shaker 3. Attachment rod 4. Gyroscope PWB.*

7.3.2 Methods for Vibration Characterization

As mentioned in earlier chapters, the majority of MEMS gyroscopes take advantage of the Coriolis force. The Coriolis force couples the drive-mode vibration to the sense-mode vibration. Sense-mode vibration is proportional to the angular velocity. Therefore MEMS gyroscopes can be very sensitive to vibrations.

At a certain, characteristic, frequency the inner structures of the MEMS gyroscopes start to resonate. This frequency is called the resonance frequency. It is an import parameter in evaluating the gyroscope performance, because at resonance frequency gyroscope starts to ring and sends arbitrary angular velocity information or no output at all. The resonance frequency can be estimated for example by doing simulations. These simulations are very similar as done in the case of shock impacts with FEM-analysis software.

The DUTs can be subjected to different vibration conditions where the waveform, frequency, duration and overall time of vibrations can be altered. The angular velocity output data can be measured during the vibrations, but it is highly unlikely that the output would be readable. That is why it is more suitable to see how the gyroscopes work after the vibration tests than continuous measurement of the angular velocity under vibration environment.

The power spectral density (PSD) is a powerful tool in characterizing random processes, such as vibration, in electronics and communication systems. Power spectral density can be used in analyzing the power density of a random or periodic signal as a function of frequency. The PSD describes how the power of a time series signal is distributed with frequency. The terminology encountered in PSD calculation often describes the signal power as relative rather than absolute values. This is because typically signals have units that causes power measures to be relative instead of absolute. Depending on the units of the signal, magnitude of power spectral density is often described as V^2/Hz, dB/Hz, W^2/Hz or G^2/Hz. [94]

The PSD function has three requirements for further analysis. The first requirement is that the PSD function, call it $S(f)$, should be a continuous signal (for integration). The second requirement is that $S(f)$ is proportional to the power of the sinusoidal signals (with frequency f) that constitute it. In other words, the power of the PSD is related to the power of the sums of the sine waves that make the PSD. The third requirement is related to the second requirement: the average signal power P_{avg} can be calculated with equation 13. This means that the integral of the power spectral density over the whole frequency range equals the average signal power (Fig. 48). [94]

$$P_{avg} = \int_{-\infty}^{\infty} S(f)\,\mathrm{d}f. \tag{13}$$

The PSD helps to estimate the frequency range or frequency points that are more interesting than the others. It can be used to estimate which frequency levels contain most of the vibration energy and are potentially more harmful

for the functionality of the gyroscopes (e.g. possible damage inflicted to the inner structures of the gyroscope).

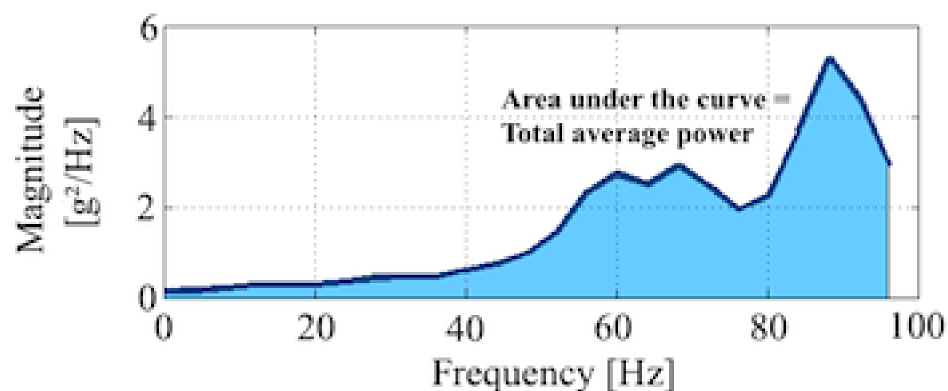

Figure 48: *Example of a PSD curve. Total average power of the signal is the area under the signal curve.*

7.3.3 Testing of Vibration Equipment

Performance of the vibration test equipment, with a small aluminum gyroscope PWB attached, was evaluated with various sine waves, sine sweep and random noise. Vibration case results are listed in Table 3. Acceleration and power spectral density (PSD) figures of the measured accelerations during the different vibration cases are presented. The Matlab code listing for PSD-calculation for one test case (10Hz) is shown in Appendix I at the end of this work. Code listings for the other test cases are analogous to this one.

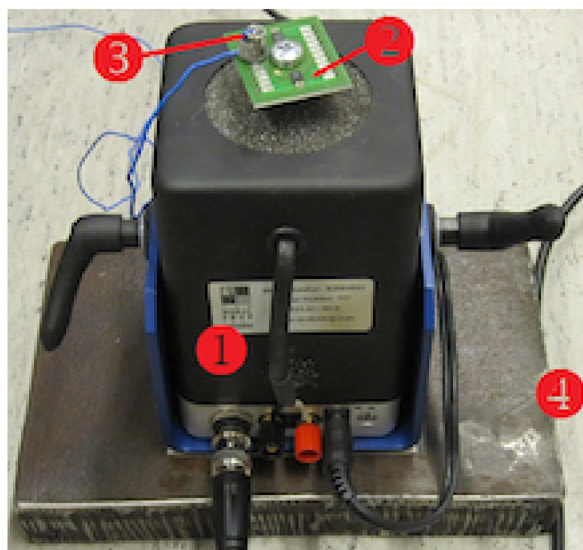

Figure 49: *Vibration shaker setup: 1. Vibration shaker 2.Gyroscope PWB 3. Accelerometer 4. Metal slab*

Vibration testing was performed with the setup presented earlier in Fig. 47, on page 57, except that the attachment rod was removed and the shaker was screwed to a metal slab weighing approximately 15kg (Fig. 49). The rod was removed so that the board could be attached as close as possible to the shaker and to remove any unwanted mass between the shaker and the gyroscope board. The metal slab keeps the shaker in-place so it does not jump about on the ground when it is set to vibrate. The accelerometer is placed near the gyroscopes on the board to measure the acceleration due to vibration. The waveform generator is not shown in Fig. 49, because it stayed essentially the same.

Testing begun with outputting sine waves from the waveform generator to the input of the shaker. The shaker vibrates according to the given input. Acceleration of the vibrated board and component was measured with a lightweight accelerometer (0,7g) mounted on top of the board near the gyroscope components. The accelerometer has a measurement range of 5000G (peak). Each sine wave case lasted for one seconds, except the last case, sine sweep, that lasted for ten seconds to cover the whole frequency range from 10Hz to 13kHz.

The acceleration and power spectral densities of the sine waves are presented in Figures 50 to 53 . In the case of 10Hz sine wave PSD (Fig. 51), the harmonic spikes can be seen clearly. Harmonics were either not present or very low for cases above 100Hz. The power spectral densities of the sine wave cases above 1000Hz were analogous to each other with narrowing width and increasing magnitude of the PSD spike clearly visible. Therefore, the figures for cases from 2000Hz to 13000kHz are not presented here. The narrowing width and increasing magnitude of the PSD spike can be seen, for example, comparing the power spectral densities of 100Hz and 1000Hz sine waves to each other (Figures 52 and 53).

The logarithmic sine sweep from 10Hz to 13kHz (Fig. 50) contained the highest peak acceleration of ~880G:s, but it had the total average energy of only $158{*}10^6 G^2$. Second highest peak accelerations were measured in 1000Hz and 3000Hz sine wave cases, where the peak acceleration was near 200G in both cases. Sine wave case of 3000Hz had the highest total average energy of $814{*}10^6 G^2$.

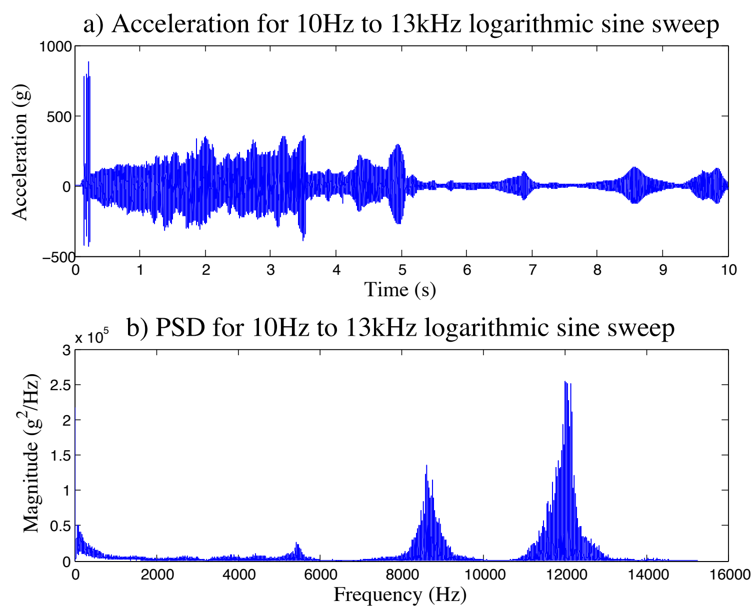

Figure 50: *Acceleration and power spectral density of the logarithmic sine sweep from 10Hz to 13kHz.*

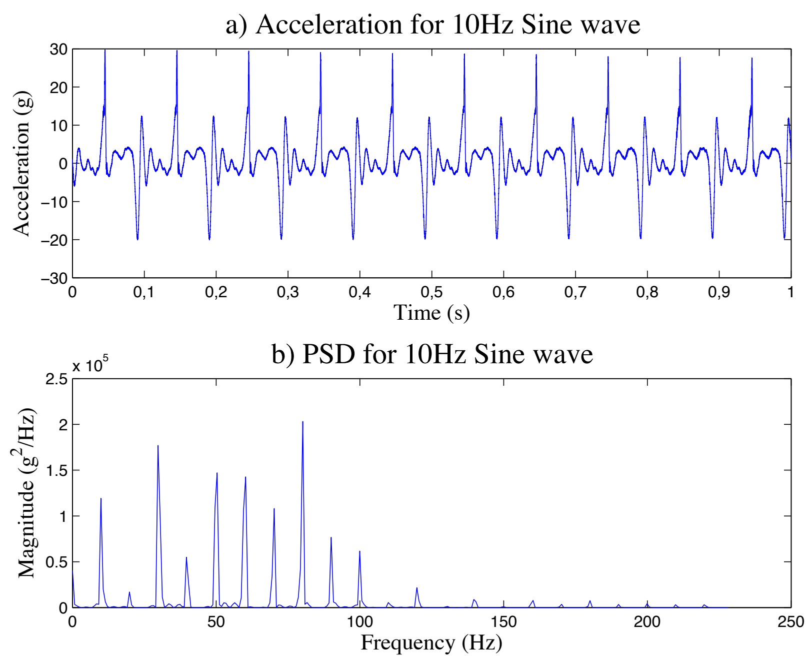

Figure 51: *Acceleration and power spectral density of 10Hz sine wave.*

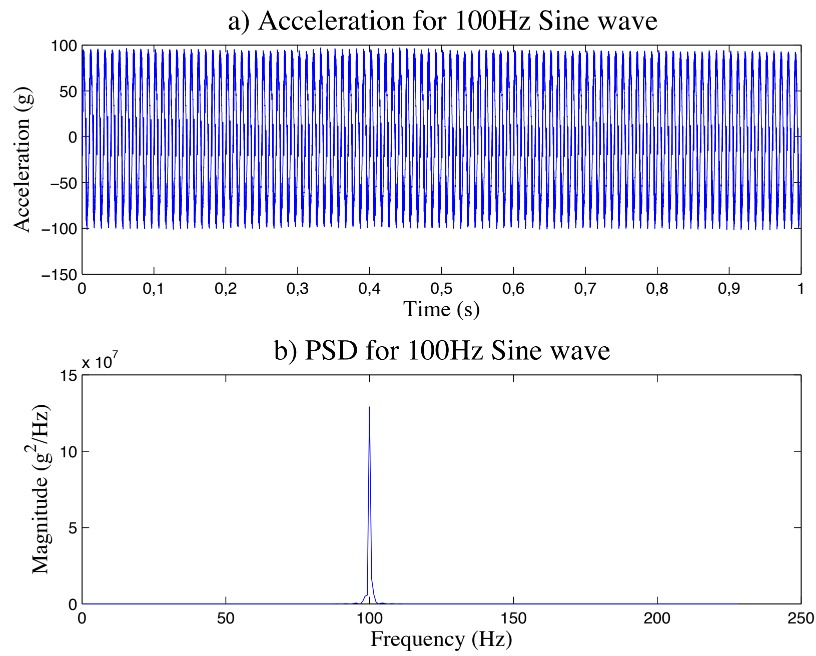

Figure 52: *Acceleration and power spectral density of 100Hz sine wave.*

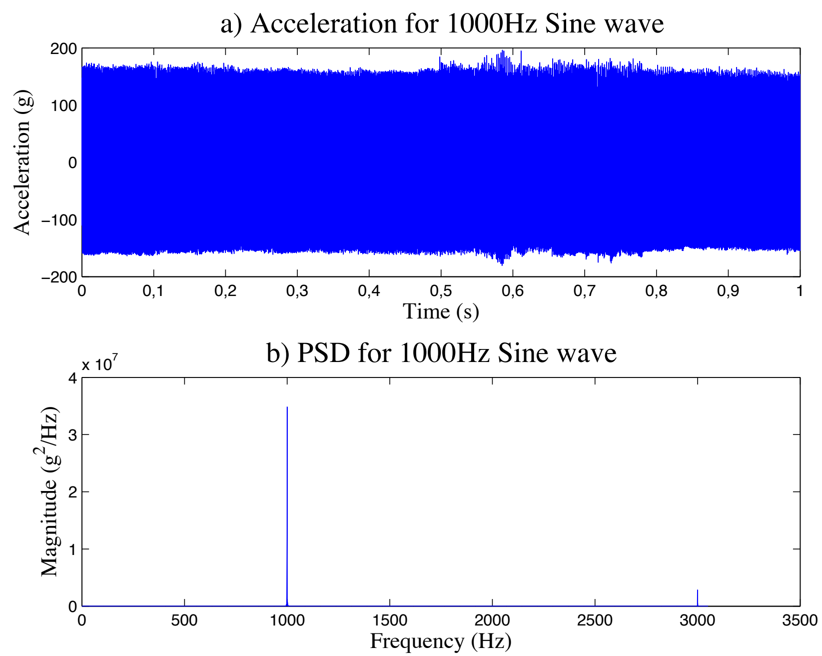

Figure 53: *Acceleration and power spectral density of 1kHz sine wave.*

The applied waveforms, their frequency, root mean square (RMS), peak acceleration and total average energy, are summarized in Table 3.

Table 3: *Results of the vibration cases.*

Applied waveform	Frequency (Hz)	RMS (G)	Peak acceleration (G)	Total average energy $*10^6$ (G^2)
Sine wave	10	6,2	29,7	2,94
Sine wave	100	59,2	97,2	267
Sine wave	1000	69,0	195,8	363
Sine wave	2000	36,6	81,0	102
Sine wave	3000	103,2	200,8	814
Sine wave	4000	21,1	46,7	40,8
Sine wave	5000	29,7	42,3	67,2
Sine wave	6000	8,5	14,8	5,56
Sine wave	13000	13,6	20,1	14,1
Sine sweep	10 to 13000	55,9	883,4	158

Based on the results it is easy to see that the magnitude (RMS and peak acceleration) of the vibration loading is significantly lower than in high-G shock impact testing. Nonetheless, vibration testing offers a possibility of very similar stresses and failure modes by adjusting the amplitude and frequency of vibration loadings. In terms of frequency, it is quite fast compared to the high-G shock impact test equipment, where the maximum impact repetition frequency is approximately 1,6Hz.

Random vibration testing was not performed with the current the equipment, because the waveform generator had a random white noise preset where the amplitude of the wave could not be adjusted. However, the waveform generator can be connected to a computer to generate random signal (or any other signal) and to properly adjust its amplitude. Random vibration is usually used to approximate real world application environments, because it allows to excite a wide range of frequencies simultaneously that add up to the total energy levels of vibration. Sine sweep, on the other hand, is strictly controlled and frequencies are excited in a predetermined order. This makes the sine sweep more ideal tool for seeking out the natural frequencies of the test equipment and the device under testing.

As seen in the PSD of the sine sweep case (Fig. 50), most of the energy is concentrated in frequencies 9000Hz and 12000Hz. These frequency spikes can be very likely the natural frequencies of the test equipment. In addition to vibration measurements, FEM simulations can be used to gain similar results, and help to determine and verify the natural frequencies of the test equipment.

8 Further Development

Further development of the rotation device is required to increase the number of testable gyroscopes and versatility of the test software. Currently the device is capable of handling 24 gyroscopes without modifications to the communication electronics (SPI-bus). Adding an multiplexer to the setup would increase the number of devices up to 30 that is the current number of gyroscopes that fit in the setup. Multiplexer makes it possible for several signals to share the same communication line, instead of having one device per input signal.

One important concern in the test software is the possibility of minor delays in reading the angular velocities. Usage of Microsoft's .NET -framework in accessing the SPI-routines is the possible cause of this hindrance, the other being the temporary loss of wireless connection to the gyroscopes (i.e. blocking the signal accidentally).

The .NET -framework uses a virtual machine that translates the pre-compiled code to a binary code that operating systems can read and execute. The translation of pre-compiled code to the binary code uses Just-in-time compilation (JIT) also known as dynamic translation. JIT causes typically a slight delay in to the initial execution of SPI- and IO-bound routines due to the time taken to load and translate the pre-compiled code. The more optimizations JIT performs, the more improved code it will generate, but the initial delay will also increase. Therefore, a JIT compiler has to make a trade-off between the quality of the code and the compilation time.

One possible solution for the root cause of these delays is to hardcode the binary SPI- and IO-bound routines rather than use the .NET -framework and JIT compilation. This obviously requires significant amount of time and effort and good knowledge of the SPI-protocol.

Another possible addition to the test software is to include the automated calculation of power spectral density (PSD) from X-Y-Z angular velocities. The power spectral density is the frequency response of a random or periodic signal. It explains where the average power is distributed as a function of frequency. This is a powerful tool to help identifying frequency dependent noise in gyroscopes. The National Instruments Labview application has a PSD calculation function as a default tool so it can be added to the test software.

9 Conclusions

Micro-electro-mechanical systems (MEMS) sensors have gained considerable popularity beyond the automotive industry and can be found in consumer applications ranging from mobile phones to video gaming consoles. The focus of this work is MEMS gyroscope sensors that are used to measure angular velocity and sense orientation. Particularly, this work describes the development of thermomechanical and mechanical characterization approaches and practical methods for the reliability assessment of digital 3-axial MEMS gyroscopes. The mechanical characterization consist of (i) high-G shock impact testing and (ii) vibration testing. The thermomechanical charaterization consists of (iii) environmental testing.

As the applications of MEMS devices for consumer markets, military, medical and space environments are progressively increasing, there is a need for new testing concepts and even new standardized tests. All aspects of the reliability engineering of MEMS devices need to be considered. The test methodology and test equipment, physics of failure, packaging, as well as computer modeling and simulations are a large part of developing reliable MEMS devices. The emphasis of this work is on the development of test equipment and methods, but the failure analyses of MEMS gyroscopes are beyond the scope of this work.

The primary objective of my Master's thesis was the design and development of test methodology for reliability characterization of MEMS gyroscopes. Requirements for the tester were arising from the low target noise level, harsh environmental conditions and the high dynamic range of the gyroscopes. The testing was also required to be automated with controllable environmental conditions such as temperature and humidity. One of the key design points was the rotating of the gyroscopes around only one axis to excite angular velocity in all three axes of the gyroscope. Thus, a rotation device was built based on a servo-motor and a stand-alone control program for the automated testing. The functionality of the environmental test setup was tested successfully with one 3-axial MEMS gyroscope at room temperature.

The mechanical characterization of the gyroscopes was performed with the high-G shock impact equipment and the vibration test equipment. The existing high-G shock impact equipment included a pneumatic shock impact tester that was modified to gain higher G-values (up to 80 000G) and a jig for fitting gyroscopes to different orientations for testing. A table-top version of the rotation device, with the same operating principle, was made also for the mechanical characterization. The functionality of the high-G shock impact equipment was verified with six measurements of different G-values and pulse widths. The gyroscopes failed in all impact cases. The vibration test equipment consisted of waveform generator and vibration shaker. The capability of the vibration test equipment was measured with the accelerometer attached near the gyroscope on top of the printed wiring board.

References

[1] Jourdan, D. Sensors Market Trends. *Sensors and Transducers e-Digest*, 2006, vol. 67, no. 5, pp. 1–100.

[2] Anscombe, N. MEMS Are on the Move in Europe. Internet Document. Updated 1.12.2003. Referenced 20.4.2011. Available: http://www.photonics.com/Article.aspx?AID=17572.

[3] MIL-STD-721C. Definition of Terms for Reliability and Maintainability. Washington DC, The US Department of Defence, 1981, 18 pp.

[4] Young, H. and Freedman, R. *University Physics with Modern Physics*. 11th edition, San Francisco, Pearson Addison-Wesley, 2004.

[5] McKean, E. *The New Oxford American Dictionary: CD-ROM*. The New Oxford American Dictionary, Oxford University Press, 2005.

[6] Turner, Glenn. History of Gyroscopes. Internet document. Updated 2011. Referenced 16.7.2011. Available: http://www.gyroscopes.org/history.asp.

[7] Britannica Online. Keyword: "Gyroscope". Internet document. Updated 22.6.2011. Referenced 20.1.2011. Available: http://www.britannica.com/EBchecked/topic/250498/gyroscope.

[8] Acar, C. and Shkel, A. *MEMS Vibratory Gyroscopes: Structural Approaches to Improve Robustness*. 2nd edition, New York, Springer-Verlag, 2008.

[9] Macek, W. and Davis, D. T. Rotation Rate Sensing with Traveling-Wave Ring Lasers. *Applied Physics Letters*, 1963, vol. 2, no. 3, pp. 67–68.

[10] Fedder, G. Fabrication, Characterization, and Analysis of a DRIE CMOS-MEMS Gyroscope. *IEEE Sensors Journal*, 2003, vol. 3, no. 5, pp. 622–631.

[11] Bernstein, J. An Overview of MEMS Inertial Sensing Technology. Internet Document. Updated 1.2.2003. Referenced 20.1.2011. Available: http://www.sensorsmag.com/sensors/acceleration-vibration/an-overview-mems-inertial-sensing-technology-970/.

[12] Yang, J., Fang, H. and Jiang, Q. Analysis of a Few Piezoelectric Gyroscopes. In: *Proceedings of the 2000 IEEE/EIA International Frequency Control Symposium and Exhibition*. 7.-9.6.2000, Kansas City, 2000, pp. 79–86.

[13] Hung, H., Chang, D. and Shih, W. Design and Simulation of a CMOS-MEMS Gyroscope with a Low-Noise Sensing Circuit. In: *Computer Communication Control and Automation (3CA), 2010 International Symposium on*. vol. 2, 5.-7.5.2010, Tainan, Taiwan, 2010, pp. 253–256.

[14] Nasiri, S. A Critical Review of MEMS Gyroscopes Technology and Commercialization Status. Internet Document. Referenced 20.1.2011. Available: http://invensense.com/mems/gyro/documents/whitepapers/MEMSGyroComp.pdf.

[15] Sharma, A., Zaman, F., Amini, B. and Ayazi, F. A High-Q In-Plane SOI Tuning Fork Gyroscope. In: *2004 Proceedings of IEEE Sensors*. vol. 1, 24.-27.10.2004, Vienna Austria, 2004, pp. 467–470.

[16] Zhong, Y., Long, T., Qian, C. and Zhen, C. A Lateral-Axis Microelectromechanical Tuning-Fork Gyroscope with Decoupled Comb Drive Operating at Atmospheric Pressure. *Journal of Microelectromechanical Systems*, 2010, vol. 19, no. 3, pp. 458–468.

[17] METU-MEMS Micro-Electro-Mechanical Systems Research and Application Center. Surface Micromachined Gyroscope. Internet Document. Referenced 20.4.2011. Available: http://www.microsystems.metu.edu.tr/gyroscope/gyroscope.html.

[18] Dyer, S. *Survey of Instrumentation and Measurement*. 1st edition, New York, John Wiley & Sons, 2001.

[19] Izmailov, E., Kolesnik, M., Osipov, A. and Akimov, A. Hemispherical Resonator Gyro Technology. Problems and Possible Ways of their Solutions. In: *6th SCI Conference on Integrated Navigation Systems*. 24.-26.5.1999, St. Petersburg, Russia, 1999, pp. 24–26.

[20] Matthews, A. and Rybak, F. Comparison of Hemispherical Resonator Gyro and Optical Gyros. *Aerospace and Electronic Systems Magazine IEEE*, 1992, vol. 7, no. 5, pp. 40–46.

[21] Rozelle, D. The Hemispherical Resonator Gyro: From Wineglass to the Planets. Internet Document. Updated 2009. Referenced 20.4.2011. Available: http://www.es.northropgrumman.com/media/whitepapers/assets/hrg.pdf.

[22] Jerebets, S. Gyro Evaluation for The Mission to Jupiter. In: *IEEE 2007 Aerospace Conference*. 3.-10.3.2007, Big Sky, Montana, 2007, pp. 1–9.

[23] Apostolyuk, V., Theory and Design of Micromechanical Vibratory Gyroscopes. In: *MEMS/NEMS*, Springer US, 2006, pp. 173–195.

[24] Wang, C. and Li, B. The Application of Wavelet Filtering on Denoising Hemispherical Resonator Gyro Signal. In: *2010 3rd International Symposium on Systems and Control in Aeronautics and Astronautics (ISSCAA)*. 8.-10.6.2010, Harbin, China, 2010, pp. 402–405.

[25] Li, B., Wu, Y. and Wang, C. The Identification and Compensation of Temperature Model for Hemispherical Resonator Gyro Signal. In: *2010*

3rd International Symposium on Systems and Control in Aeronautics and Astronautics (ISSCAA). 8.-10.6.2010, Harbin, China, 2010, pp. 398–401.

[26] Shen, B., Yi, G. and Wang, C. An Extended Kalman Particle Filtering Algorithm for HRG-Based Strapdown Inertial Attitude Determination System. *Journal of Astronautics*, 2008, vol. -, no. 2, pp. 620–624.

[27] Wang, H., Yi, G., Shen, B. and Jiang, W. Research on HRG System Based on Virtual Instrument. In: *2006 1st International Symposium on Systems and Control in Aerospace and Astronautics*. 19.-21.1.2006, Harbin, China, 2006, pp. 114–118.

[28] Gao, S. and Wu, J. Theory and Finite Element Analysis of HRG. In: *Proceedings of the 2007 IEEE International Conference on Mechatronics and Automation*. 5.-8.4.2007, Harbin, China, 2007, pp. 2768–2772.

[29] Yao, Y., Gao, Z., Zhang, R., Dong, Y. and Chen, Z. A Silicon Wafer Dissolved Vibrating Gyroscope. In: *IMTC/98 IEEE Conference Proceedings Instrumentation and Measurement Technology Conference*. vol. 2, 8.-21.5.1998, St. Paul, Minnesota, 1998, pp. 1133–1136.

[30] Dong, Y., Gao, Z., Zhang, R. and Chen, Z. A Vibrating Wheel Micromachined Gyroscope for Commercial and Automotive Applications. In: *Proceedings of the 16th IEEE IMTC/99 Instrumentation and Measurement Technology Conference*. vol. 3, 24.-26.5.1999, Venice, Italy, 1999, pp. 1750–1754.

[31] Feng, Z. and Gore, K. Dynamic Characteristics of Vibratory Gyroscopes. *IEEE Sensors Journal*, 2004, vol. 4, no. 1, pp. 80–84.

[32] Greiff, P., Antkowiak, B., Campbell, J. and Petrovich, A. Vibrating Wheel Micromechanical Gyro. In: *IEEE 1996 Position Location and Navigation Symposium PLANS'96*. 22.-26.4.1996, Atlanta, Georgia, USA, 1996, pp. 31–37.

[33] Zhao, Q., Liu, X., Lin, L., Guo, Z., Cui, J., Chi, X., Yang, Z. and Yan, G. A Doubly Decoupled Micromachined Vibrating Wheel Gyroscope. In: *TRANSDUCERS 2009 Solid-State Sensors, Actuators and Microsystems Conference*. 21.-25.6.2009, Denver, Colorado, 2009, pp. 296–299.

[34] Witvrouw, A., Mehta, A., Verbist, A., Du Bois, B., Van Aerde, S., Ramos-Martos, J., Ceballos, J., Ragel, A., Mora, J., Lagos, M., Arias, A., Hinoiosa, J., Spengler, J., Leinenbach, C., Fuchs, T. and Kronmuller, S. Processing of MEMS Gyroscopes on Top of CMOS ICs. In: *IEEE International 2005 Solid-State Circuits Conference*. vol. 1, 20.2.2005, San Francisco, California, 2005, pp. 88–89.

[35] Yang, J. Analysis of Ceramic Thickness Shear Piezoelectric Gyroscopes. In: *1996 IEEE Proceedings Ultrasonic Symposium.* vol. 2, 3.-6.11.1996, San Antonio, Texas, 1996, pp. 909–912.

[36] Abe, H., Yoshida, T. and Watanabe, H. Energy Trapping of Thickness-Shear Vibrations Excited by Parallel Electric Field and Its Application to Piezoelectric Vibratory Gyroscopes. In: *1998 IEEE Proceedings Ultrasonic Symposium.* vol. 1, 5.-8.10.1998, Sendai, Miyagi, Japan, 1996, pp. 467–471.

[37] Kagawa, Y., Tsuchiya, T. and Kawashima, T. Finite Element Simulation of Piezoelectric Vibrator Gyroscopes. *IEEE Transactions on Ultrasonics, Ferroelectrics and Frequency Control*, 1996, vol. 43, no. 4, pp. 509–518.

[38] Yang, J. Some Analytical Results on Piezoelectric Gyroscopes. In: *1998 IEEE Proceedings of The Frequency Control Symposium.* 27.-29.5.1998, Pasadena, California, 1998, pp. 733–741.

[39] Kagawa, Y., Tsuchiya, T. and Sakai, T. Three-Dimensional Finite Element Simulation of a Piezoelectric Vibrator Under Gyration. *IEEE Transactions on Ultrasonics, Ferroelectrics and Frequency Control*, 2001, vol. 48, no. 1, pp. 180–188.

[40] Abe, H., Ishikawa, T. and Watanabe, H. Trapped-Energy Vibratory Gyroscopes Using a Partially-Polarized Piezoelectric Ceramic Plate with Plano-Mesa Structure. In: *2000 IEEE Proceedings of the 12th International Symposium on Applications of Ferroelectrics.* vol. 1, 21.7.-2.8.2000, Honolulu, Hawaii, 2000, pp. 93–96.

[41] Yang, J., Fang, H. and Jiang, Q. Analysis of a Plate Piezoelectric Gyroscope by Equations for a Piezoelectric Parallelepiped. In: *1999 Proceedings of the IEEE International Frequency Control Symposium* . vol. 1, 13.4.-16.4.1999, Besancon, France, 1999, pp. 433–436.

[42] He, G., Nguyen, C., Hui, J., Wong, M., Ng, A., Luong, H. and Ling, C. A Piezoelectric-Plate Microgyroscope. In: *Proceedings of International Solid State Sensors and Actuators Conference (Transducers '97).* 16.-19.6.1997, Chicago, Illinois, 1997, pp. 895–898.

[43] Pat-US7159441B2. Cloverleaf Microgyroscope with Electrostatic Alignment and Tuning. The Boeing Company, Chicago, USA. (Challoner et al.) US10/843139, 11.5.2004. Publ. 9.1.2007. 11 pp.

[44] Tang, T., Gutierrez, R., Wilcox, J., Stell, C., Vorperian, V., Calvet, R., Li, W., Charkaborty, I., Bartman, R. and Kaiser, W. Silicon Bulk Micromachined Vibratory Gyroscope. In: *Tech. Dig. Solid-State Sensor and Actuator Workshop.* 3.-6.6.1996, Hilton Head Island, South Carolina, 1999, pp. 288–293.

[45] Tang, T., Gutierrez, R., Stell, C., Vorperian, V., Arakaki, G., Rice, J., Li, W., Chakraborty, I., Shcheglov, K. and Wilcox, J. A Packaged Silicon MEMS Vibratory Gyroscope for Microspacecraft. In: *Proceedings IEEE The Tenth Annual International Workshop on Micro Electro Mechanical Systems*. 26.-30.1.1997, Nagoya, Japan, 1997, pp. 500–505.

[46] Bae, S., Hayworth, K., Yee, K., Shcheglov, K., Challoner, A. and Wiberg, D. High Performance MEMS Micro-Gyroscope. In: *Symposium on Design, Test, Integration, and Packaging Proceeding CAD, Design and Test Conference*. 5.-8.5.2002, Cannes-Mandelieu, France, 2002, pp. 316–324.

[47] Maenaka, K., Sawai, N., Ioku, S., Sugimoto, H., Suzuki, H., Fujita, T. and Takayama, Y. MEMS Gyroscope with Double Gimbal Structure. In: *Transducers 12th International Conference on Solid-State Sensors, Actuators and Microsystems*. vol. 1, 8.-12.6.2003, Boston, USA, 2003, pp. 163–166.

[48] Apostolyuk, V., Logeeswaran, V. and Tay, F. Efficient Design of Micromechanical Gyroscopes. *Journal of Micromechanics and Microengineering*, 2002, vol. 12, no. 6, pp. 948–954.

[49] Lobur, M. and Holovatyy, A. Overview and Analysis of Readout Circuits for Capacitive Sensing in MEMS Gyroscopes (MEMS Angular Velocity Sensors). In: *MEMSTECH 2009 5th International Conference on Perspective Technologies and Methods in MEMS Design*. 22.-24.4.2009, Lviv-Polyana, Ukraine, 2009, pp. 161–163.

[50] Song, Z., Chen, X., Huang, S., Wang, Y., Jiao, J. and Li, X. A High-Sensitivity Piezoresistive Gyroscope with Torsional Actuation and Axially-Stressed Detection. In: *Proceedings of IEEE Sensors*. 22.-24.10.2003, Toronto, Canada, 2003, pp. 457–460.

[51] Li, X., Chen, X., Song, Z., Dong, P., Wang, Y., Jiao, J. and Yang, H. A Microgyroscope With Piezoresistance for Both High-Performance Coriolis-Effect Detection and Seesaw-Like Vibration Control. *Journal of Microelectromechanical Systems*, 2006, vol. 15, no. 6, pp. 1698–1707.

[52] Bao, M.-H. and Middelhoek, S. *Micro Mechanical Transducers - Pressure Sensors, Accelerometers and Gyroscopes*. 1st edition, New York, Elsevier, 2000.

[53] Gunthner, S., Kapser, K., Rose, M., Hartmann, B., Kluge, M., Schmid, U. and Seidel, H. Analysis of Piezo-Resistive Read-Out Signals for a Silicon Tuning Fork Gyroscope. In: *2004 Proceedings of IEEE Sensors*. 24.-27.10.2004, Vienna, Austria, 2004, pp. 1411–1414.

[54] Gunthner, S., Egretzberger, M., Kugi, A., Kapser, K., Hartmann, B., Schmid, U. and Seidel, H. Compensation of Parasitic Effects for a Silicon

Tuning Fork Gyroscope. *IEEE Sensors Journal*, 2006, vol. 6, no. 3, pp. 596–604.

[55] Faucheux, M., Fayoux, D. and Roland, J. The Ring Laser Gyro. *Journal Optics*, 1988, vol. 19, no. 3, pp. 101–115.

[56] Pavlath, G. Fiber-Optic Gyroscopes. In: *IEEE Lasers and Electro-Optics Society (LEOS) Annual Meeting. LEOS '94 Conference Proceedings.* vol. 2, 31.10.-3.11.1994, Boston, Massachusetts, 1994, pp. 237–238.

[57] Arditty, H. and Lefevre, H. Sagnac Effect in Fiber Gyroscopes. *Optics Letters*, 1981, vol. 6, no. 8, pp. 401–403.

[58] Jianqiang, Y., Xueqing, J. and Baolun, Y. Digital Detection and Control System for Ring Laser Gyro. In: *2010 2nd International Conference on Advanced Computer Control (ICACC).* vol. 3, 27.-29.3.2010, Shenyang, China, 2010, pp. 216–220.

[59] Banerjee, K., Dam, B., Majumdar, K., Banerjee, R. and Patranabis, D. An Improved Dither-Stripping Scheme for Strapdown Ring Laser Gyroscopes. In: *TENCON 2004 IEEE Region 10 Conference.* 24.-24.9.2004, Chiang Mai, Thailand, 2004, pp. 689 – 692.

[60] Zhang, W., Song, Z., Yang, M. and Y.Z., C. Smart Sensor Based on Fiber Optic Gyroscope. In: *2011 International Conference on Intelligent Computation Technology and Automation (ICICTA).* vol. 2, 28.-29.3.2011, Shenzhen, China, 2011, pp. 702–705.

[61] Neubrex Technologies. FOG principle. Internet Document. Referenced 26.4.2011. Available: http://www.neubrex.com/htm/applications/gyro-principle.htm.

[62] Spearing, S. Materials Issues in Microelectromechanical Systems (MEMS). *Acta Materialia*, 2000, vol. 48, no. 1, pp. 179–196.

[63] Judy, J. Biomedical Applications of MEMS. In: *Measurement Science and Technology Conference.* 20.-22.1.2000, Anaheim, California, 2000, pp. 403–414.

[64] Alper, S. and Akin, T. A Single-Crystal Silicon Symmetrical and Decoupled MEMS Gyroscope on an Insulating Substrate. *Journal of Microelectromechanical Systems*, 2005, vol. 14, no. 4, pp. 707–717.

[65] Jadaan, O., Nemeth, N., Bagdahn, J. and Sharpe, W. Probablistic Weibull Behavior and Mechanical Properties of MEMS Brittle Materials. *Journal of materials science*, 2003, vol. 38, no. 20, pp. 4087–4113.

[66] Lawes, R. Manufacturing Costs for Microsystems/MEMS Using High Aspect Ratio Microfabrication Techniques. *Microsystem Technologies*, 2006, vol. 13, no. 1, pp. 85–95.

[67] Samper, V. and Trigg, A. MEMS Failure Analysis and Reliability. In: *The proceedings of the 10th international symposium on the physical and failure analysis of integrated circuits (IPFA)*. 7.-11.7.2003, Singapore, 2003, pp. 17–24.

[68] van Spengen, W. M., Puers, R. and De Wolf, I. On the Physics of Stiction and Its Impact on the Reliability of Microstructures. *Adhesion Sci. Technol.*, 2003, vol. 17, no. 4, pp. 563–582.

[69] Ramesham, R. and Ghaffarian, R. Challenges in Interconnection and Packaging of Microelectromechanical Systems (MEMS). In: *2000 Proceedings. 50th Electronic Components and Technology Conference*. 21.-24.5.2000, Las Vegas, 2000, pp. 666–675.

[70] van Spengen, W. MEMS Reliability from a Failure Mechanisms Perspective. *Microelectronics Reliability*, 2003, vol. 43, pp. 1049–1060.

[71] Tanner, D., Walraven, J., Helgesen, K., Irwin, L., Gregory, D., Stake, R. and Smith, N. MEMS Reliability in a Vibration Environment. In: *Reliability Physics Symposium, 2000. 38th Annual IEEE International Proceedings*. vol. 2, 10.-13.4.2000, San Jose, California, 2000, pp. 139–145.

[72] Walraven, J. Failure Analysis Issues in Microelectromechanical Systems (MEMS). *Microelectronics Reliability*, 2003, vol. 45, pp. 1750–1757.

[73] De Wolf, I. Instrumentation and Methodology for MEMS Testing, Reliability Assessment and Failure Analysis. In: *24th International Conference on Microelectronics*. vol. 1, 16.-19.5.2004, Niš, Serbia and Montenegro, 2004, pp. 57–63.

[74] Choa, S. Reliability of Vacuum Packaged MEMS Gyroscopes. *Microelectronics and Reliability*, 2005, vol. 45, pp. 361–369.

[75] Tan, L. B., Ang, C. W., Lim, C. T., Tan, V. and Zhang, X. Modal and Impact Analysis of Modern Portable Electronic Products. In: *The proceedings of the 55th Electronic Component and Technology Conference*. 31.5.-3.6.2005, Lake Buena Vista, Florida, 2005, pp. 645–653.

[76] Yang, C., Zhang, B., Chen, D. and Lin, L. Drop-Shock Dynamic Analysis of MEMS/Package System. In: *The proceedings of the 23rd International Conference on Micro Electro Mechanical Systems (MEMS)*. 24.-28.1.2010, Wanchai, Hong Kong, 2010, pp. 24–28.

[77] JESD22-B111. Board Level Drop Test Method of Components for Handheld Electronics Products. Arlington VA, JEDEC Solid State Technology Association, 2003, 14 pp.

[78] JESD22-B104C. Mechanical Shock. Arlington VA, JEDEC Solid State Technology Association, 2004, 12 pp.

[79] Hauck, T., Li, G., McNeill, A., Knoll, H., Ebert, M. and Bagdahn, J. Drop Simulation and Stress Analysis of MEMS Devices. In: *The proceedings of the 7th International conference on Thermal, Mechanical and Multiphysics Simulation and Experiments in Micro-Electronics and Micro-Systems (EuroSimE)*. 24.-26.4.2006, Como, Italy, 2006, pp. 1–5.

[80] Srikar, V. and Senturia, S. The Reliability of Microelectromechanical Systems (MEMS) in Shock Environments. *Journal of Microelectromechanical Systems*, 2002, vol. 11, no. 3, pp. 206–214.

[81] Comsol. Estimating the Q Factor of a MEMS Gyroscope. Internet Document. Referenced 28.4.2011. Available: http://www.comsol.com/showroom/gallery/2186/.

[82] Wagner, U., Franz, J., Schweiker, M., Bernhard, W., Müller-Fiedler, R., Michel, B. and Paul, O. Mechanical Reliability of MEMS-Structures Under Shock Load. *Microelectronics and Reliability*, 2001, vol. 41, no. -, pp. 1657–1662.

[83] Weber, M., Bellrichard, M. and Kennedy, C. High Angular Rate and High G Effects in the MEMS Gyro. *Sensors Magazine*, 2004, vol. -, no. -, pp. 1–5.

[84] Brown, T. Harsh Military Environments and Microelectromechanical (MEMS) devices. In: *Proceedings of IEEE Sensors 2003*. vol. 2, 22.-24.10.2003, Toronto, Canada, 2003, pp. 753–760.

[85] Brown, T. G., Davis, B., Hepner, D., Faust, J., Myers, C., Muller, P., Harkins, T., Hollis, M., Miller, C. and Placzankis, B. Strap-Down Microelectromechanical (MEMS) Sensors for High-G Munition Applications. *IEEE Transactions on Magnetics*, 2001, vol. 37, pp. 336–342.

[86] Dean, R., Flowers, G., Hoodel, A., Roth, G., Castro, S., Zhou, R., Moreira, A., Ahmed, A. and Rifki, R. On the Degradation of MEMS Gyroscope Performance in the Presence of High Power Acoustic Noise. In: *IEEE International Symposium on Industrial Electronics*. 4.-7.6.2007, Vigo, Spain, 2007, pp. 1435–1440.

[87] Bazu, M., Galateanu, L., Ilian, V., Loicq, J., Habraken, S. and Colette, J.-P. Reliability Accelerated Testing of MEMS Accelerometers. In: *International Semiconductor Conference CAS 2007*. vol. 1, 15.-17.10.2007, Sinaia, Romania, 2007, pp. 103–106.

[88] Shcheglov, K., Evans, C., Gutierrez, R. and Tang, T. Temperature Dependent Characteristics of the JPL Silicon MEMS gyroscope. In: *IEEE Aerospace Conference Proceedings 2000*. vol. 1, 18.-25.3.2000, Big Sky, Montana, 2000, pp. 403–411.

[89] Patel, C., McCluskey, P. and Lemus, D. Performance and Reliability of MEMS Gyroscopes at High Temperatures. In: *12th IEEE Intersociety Conference on Thermal and Thermomechanical Phenomena in Electronic Systems (ITherm)*. 2.-5.6.2010, Las Vegas, Nevada, 2010, pp. 1–5.

[90] Esfandyari, J., Nuccio, R. and Xu, G. Introduction to MEMS gyroscopes. Internet Document. Updated 15.11.2010. Referenced 14.5.2011. Available: http://www.electroiq.com/articles/stm/2010/11/introduction-to-mems-gyroscopes.html.

[91] Alper, S., Azgin, K. and Akin, T. A High-Performance Silicon-On-Insulator MEMS Gyroscope Operating at Atmospheric Pressure. *Sensors and Actuators. A, Physical*, 2007, vol. 135, no. 1, pp. 34–42.

[92] Tipler, P. and Mosca, G. *Physics for Scientists and Engineers*, vol. 1. 6th edition, New York, Worth Publishers, 2008.

[93] Hokka, J., Mattila, T., Li, J., Teeri, J. and Kivilahti, J. A Novel Impact Test System for More Efficient Reliability Testing. *Microelectronics Reliability*, 2010, vol. 50, no. 8, pp. 1125–1133.

[94] Howard, R. *Principles of Random Signal Analysis and Low Noise Design - The Power Spectral Density and Its Application.* 1st edition, New York, Wiley-IEEE Press, 2002.

Appendix I

This appendix contains the Matlab code listing for Power Spectral Density calculation used in Chapter 7.3.3.

```
load 10Hz_sine_1s.txt; y = X10Hz_sine_1s(:,1);
a = 'fontsize'; b = 'fontname';

% number of FFT points, power of 2
nfft = 2^nextpow2(length(y));

% sampling frequency and time between samples
Fs = 100000;
deltat = 1/Fs;

% calculating DFT
Y = fft(y, nfft);

% calculating PSD, power of different frequencies in signal
Pyy= Y.*conj(Y) / nfft;

% calculating frequency vector, number of frequency/FFT points
f=Fs*(0:nfft-1)/nfft;

% calculating RMS values
RMS=sqrt(sum(y.*conj(y))/size(y,1))

% calculating peak values
Peak=max(y)

% calculating total average energy
Energy = trapz(f, Pyy)

subplot(2,1,1) plot(y)
xlabel('Time (s)','fontsize',14,'fontname','Times')
ylabel('Acceleration (g)',a,14,b,'Times')
title('a) Acceleration for 10Hz Sine wave',a,18,b,'Times')
set(gca,'XTickLabel','0|0,1|0,2|0,3|0,4|0,5|0,6|0,7|0,8|0,9|1')

subplot(2,1,2) plot(f(1:300),Pyy(1:300))
xlabel('Frequency (Hz)',a,14,b,'Times')
ylabel('Magnitude (g^2/Hz)',a,14,b,'Times')
title('b) PSD for 10Hz Sine wave',a,18,b,'Times')
```

Appendix II

This appendix contains the image of the second failed gyroscope from Chapter 7.2.3.

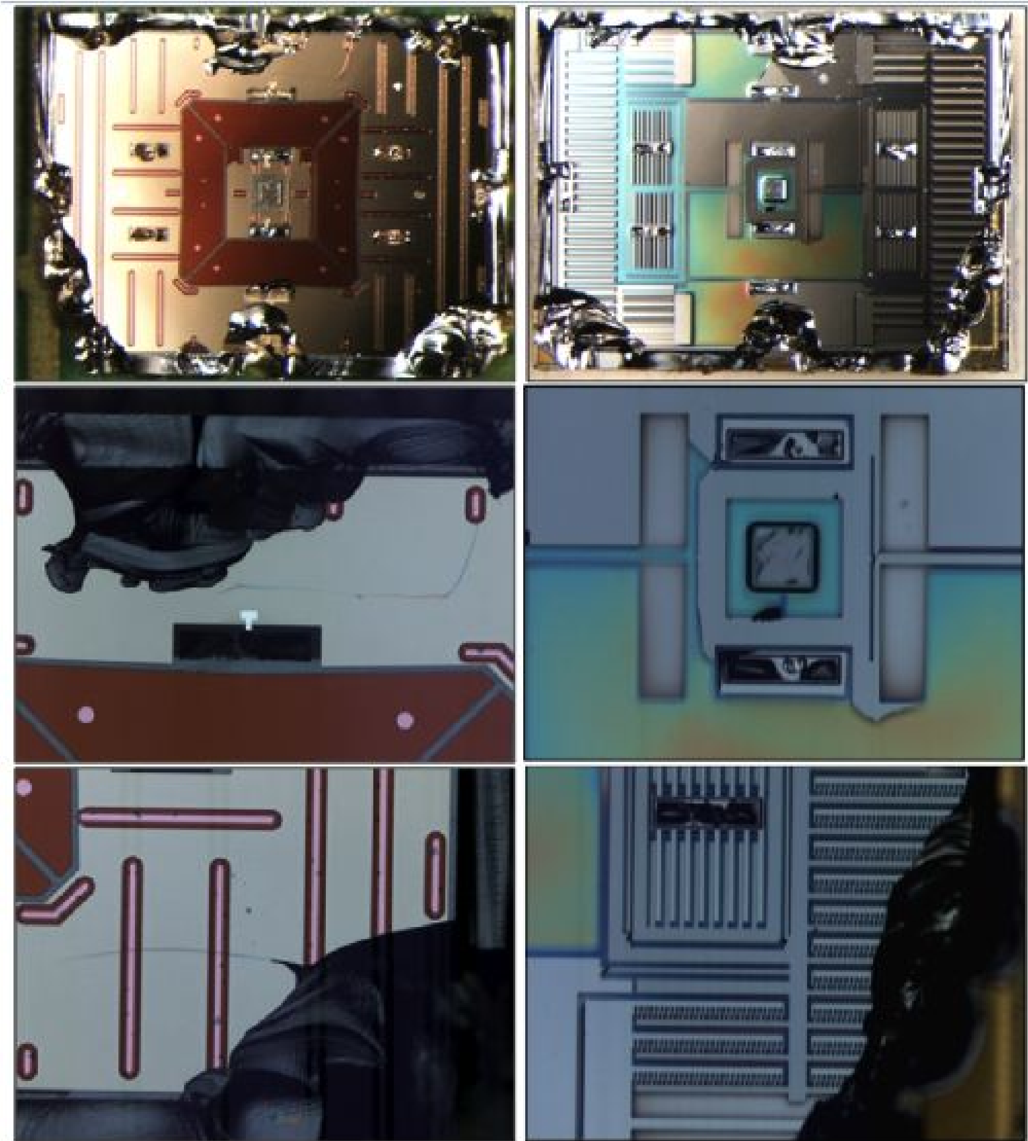

Figure 54: *The failed structure of gyroscope 2. The left-hand column is the structure that stayed attached to the board and the right-hand column the structure that broke-off.*

Appendix III

This appendix contains the image of the third failed gyroscope from Chapter 7.2.3.

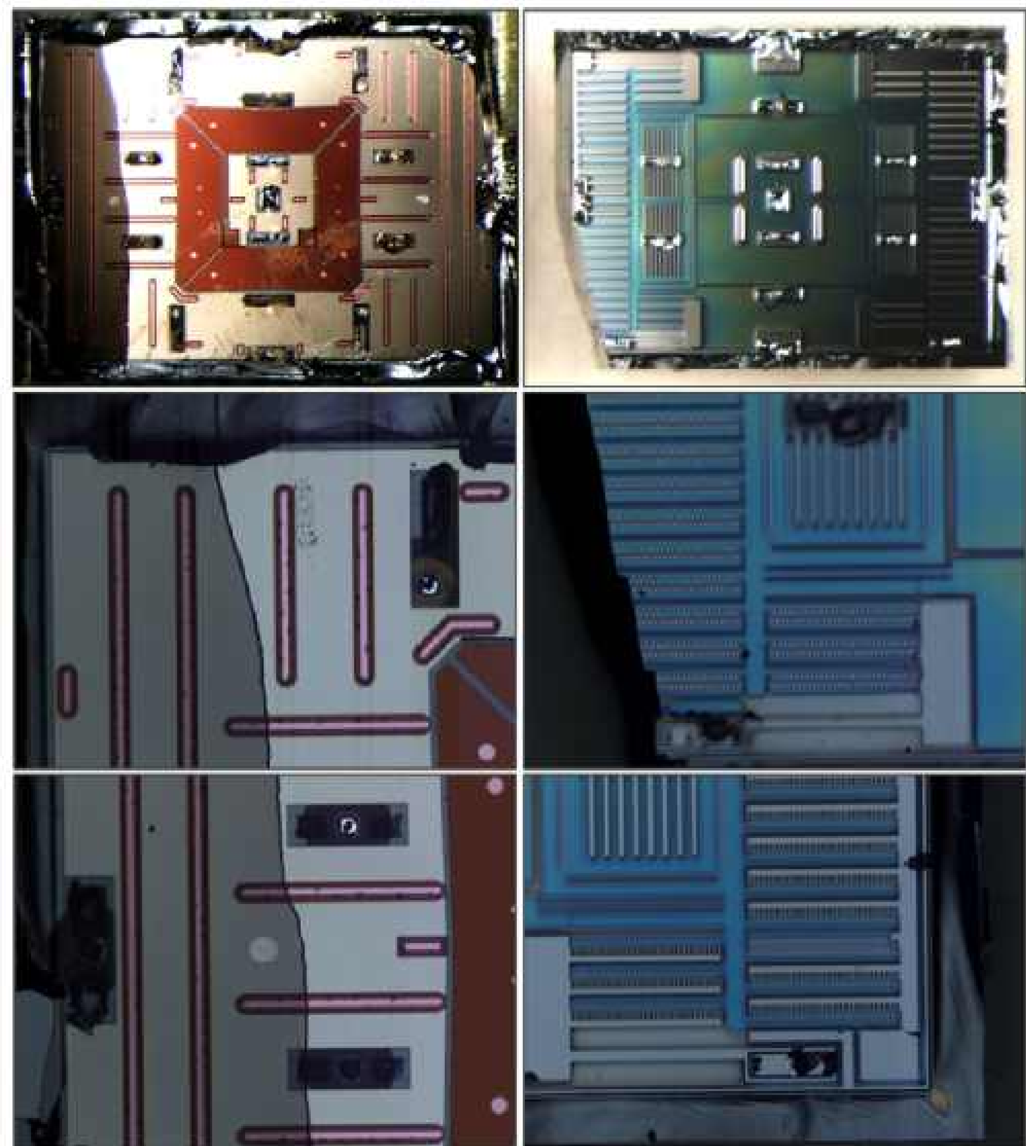

Figure 55: *The failed structure of gyroscope 3. The left-hand column is the structure that stayed attached to the board and the right-hand column the structure that broke-off.*